



**HAL**  
open science

# Seismic Fragility Analysis based on Artificial Ground Motions and Surrogate Modeling of Validated Structural Simulators

G. Abbiati, M. Broccardo, Iman Abdallah, S. Marelli, F. Paolacci

► **To cite this version:**

G. Abbiati, M. Broccardo, Iman Abdallah, S. Marelli, F. Paolacci. Seismic Fragility Analysis based on Artificial Ground Motions and Surrogate Modeling of Validated Structural Simulators. 2021. hal-03138932

**HAL Id: hal-03138932**

**<https://hal.science/hal-03138932v1>**

Preprint submitted on 11 Feb 2021

**HAL** is a multi-disciplinary open access archive for the deposit and dissemination of scientific research documents, whether they are published or not. The documents may come from teaching and research institutions in France or abroad, or from public or private research centers.

L'archive ouverte pluridisciplinaire **HAL**, est destinée au dépôt et à la diffusion de documents scientifiques de niveau recherche, publiés ou non, émanant des établissements d'enseignement et de recherche français ou étrangers, des laboratoires publics ou privés.

# SEISMIC FRAGILITY ANALYSIS BASED ON ARTIFICIAL GROUND MOTIONS AND SURROGATE MODELING OF VALIDATED STRUCTURAL SIMULATORS

G. Abbiati, M. Broccardo, I. Abdallah, S. Marelli, F. Paolacci



## Data Sheet

---

**Journal:** -  
**Report Ref.:** RSUQ-2020-013  
**Arxiv Ref.:** -  
**DOI:** -  
**Date submitted:** 17/07/2020  
**Date accepted:** -

---

# Seismic Fragility Analysis based on Artificial Ground Motions and Surrogate Modeling of Validated Structural Simulators

G. Abbiati<sup>\*1</sup>, M. Broccardo<sup>2</sup>, I. Abdallah<sup>3</sup>, S. Marelli<sup>3</sup>, and F. Paolacci<sup>4</sup>

<sup>1</sup>*Department of Engineering, Aarhus University, Denmark*

<sup>2</sup>*Department of Civil, Environmental and Mechanical Engineering, University of Trento, Italy*

<sup>3</sup>*Department of Civil, Environmental and Geomatic Engineering, ETH Zurich, Switzerland*

<sup>4</sup>*Department of Engineering, Roma Tre University, Italy*

Draft submitted to *engrXiv*

January 23, 2021

## Abstract

This study introduces a computational framework for efficient and accurate seismic fragility analysis based on a combination of artificial ground motion modeling, polynomial-chaos-based global sensitivity analysis, and hierarchical kriging surrogate modeling. The framework follows the philosophy of the Performance-Based Earthquake Engineering PEER approach, where the fragility analysis is decoupled from hazard analysis. This study addresses three criticalities that are present in the current practice. Namely, reduced size of hazard-consistent size-specific ensembles of seismic records, validation of structural simulators against large-scale experiments, high computational cost for accurate fragility estimates. The effectiveness of the proposed framework is demonstrated for the Rio Torto Bridge, recently tested using hybrid simulation within the RETRO project.

**Keywords:** Fragility analysis ; surrogate modeling ; hierarchical kriging ; polynomial chaos expansion ; global sensitivity analysis ; artificial ground motion.

## 1 Introduction

The PEER Performance-Based Earthquake Engineering (PBEE) framework is widely used to perform seismic risk analysis. The framework is an implementation of total probability theorem, which combines the output of Probabilistic Seismic Hazard Analysis (PSHA) with fragility, damage, and loss analysis. A critical part of the framework is the coupling between hazard and structural modeling, namely, fragility analysis. It comes as no surprise that it developed into a stand-alone research field. Given a structural system of interest, the most recent advancement in fragility analysis requires the selection of a set of suitable ground motions to be used as input for non-linear structural analysis. Then, the statistics of a Quantity of Interest (QoI), which in general is denoted as Engineering Demand Parameter (EDP), are derived as a function of a given Intensity Measure (IM), or a vector of IMs. Specifically, these conditional EDP-IM relations are named fragility functions. Following this line, in recent years, a lot of research has been devoted to creating computational fragility frameworks, including the selection and the use of real seismic

---

\*Corresponding Author: Dr. Giuseppe Abbiati, [abbiati@eng.au.dk](mailto:abbiati@eng.au.dk), ORCID: [0000-0002-5048-8505](https://orcid.org/0000-0002-5048-8505).

records and non-linear time history analysis. An incomplete list of studies in this topic includes (Vamvatsikos and Cornell, 2002; Porter et al., 2007; Baker, 2015; Noh et al., 2015). However, within this perimeter, a number of open issues have been raised by the opinion paper of Bradley (Bradley, 2013) and further elaborated in the state-of-the-art review of Silva and co-authors (Silva et al., 2019). Departing from these studies, this paper aims to address three criticalities:

1. In recent years, there have been significant advancements in ground motion selection procedures, which have partially solved the problem of defining a suitable set of seismic records for structural analysis. However, although these selections are sufficient to describe important characteristics of the hazard for a given structure of interest, the number of available records is usually insufficient to compute accurate estimates of the QoIs statistics.
2. The validation of structural simulators and the quantification of the associated model uncertainty against representative experiments—despite being critical—is often overlooked. This is due to practical reasons. Structural testing is usually not affordable beyond the component level due to the limited capacity of experimental facilities. Also, the budget allocated for structural testing is typically sufficient for running a small number of destructive experimental tests, which cannot cover the entire range of IMs for the fragility analysis.
3. The computation of fragility analysis requires a large number of time history analyses. It follows that computational cost of structural simulators limits *de facto* the total number of simulations. This is a classical problem in simulation-based Uncertainty Quantification (UQ), which is tackled by replacing the computationally expensive simulator with an equivalent (with respect to, w.r.t., the QoI) response surface a.k.a. surrogate model. However, defining surrogate models for non-linear dynamic analysis is challenging and still not completely addressed by the current state of the art of fragility computation. As a consequence, the accuracy of the fragility is limited by available computational resources.

This study introduces a computational framework for efficient and accurate seismic fragility analysis based on a combination of artificial ground motion modeling and surrogate modeling. Moreover, the goal is to integrate the know-how developed in ground motion selection and to follow the original spirit of the PEER-PBEE framework to decouple the task of hazard and fragility analysis. Specifically, given a suitable set of real seismic time series, we define an artificial ground motion model equipped with engineering-meaningful parameters. The selected real seismic time series are thought of as realizations of the ground motion model, using the same philosophy introduced by (Rezaeian and Der Kiureghian, 2008, 2010). Unlike their work, this framework uses the real seismic time series to calibrate the parameters of the artificial ground motion model and the associated uncertainties. The definition of such a hazard model constitutes the basis for using a surrogate-based UQ forward analysis.

The building blocks of the computational framework are: the artificial ground motion model, an expensive-to-evaluate High-Fidelity (HF) structural simulator of the reference structure *validated* against experiments (e.g., Hybrid Simulation (HS) in the proposed application (Schellenberg et al., 2009)), and a corresponding cheaper Low-Fidelity (LF) structural simulator (e.g., obtained via dynamic substructuring of the HF simulator in this study (de Klerk et al., 2008)). The seismic vulnerability analysis follows these sequential steps: i) generation of a family of artificial motions (compatible with the real selected ones); ii) computation of the Polynomial Chaos Expansion (PCE) of the LF simulator QoI prediction; iii) dimensionality reduction of the artificial ground motion parameters based on Global Sensitivity Analysis (GSA); iv) computation of a multi-fidelity (MF) surrogate based on Hierarchical Kriging (HK) that fuses LF and HF predictions of the QoI; v) the fragility analysis is derived as a natural byproduct of the framework.

Fragility analysis and, more broadly, seismic risk assessment based on stochastic simulations is not new, and an incomplete list of studies includes (Mai et al., 2017; Zentner, 2017; Trevlopoulos et al., 2019; Altieri and Patelli, 2020). Moreover, to the best of our knowledge, the first study using also kriging surrogate modeling is (Gidaris et al., 2015) and more recently (Ghosh et al., 2019). Different from the previous contributions, this paper draws a direct link between ground motion selection and the calibration of the stochastic hazard model; moreover, it introduces HK to combine predictions of simulators with different degrees of fidelity. In essence, the artificial ground motion model is used to build a large ensemble of time series, which would not be possible to compose using records of real seismic events. Therefore, this study aims to bridge classical seismic fragility analysis with the most recent UQ advancements, and not to solve the full seismic risk analysis (as done in (Gidaris et al., 2015) by fully employing the philosophy of (Rezaeian and Der Kiureghian, 2010)). In this context, this paper introduces a combination of PCE-based GSA and HK so that the computational burden associated with the fragility analysis is drastically reduced.

The framework is applied to a real-world application consisting of a Reinforced Concrete (RC) bridge case study, which was recently tested within the RETRO project (Paolacci et al., 2014; Abbiati et al., 2015). LF and HF simulators are introduced, highlighting the crucial role of HS in enabling experimental validation of the bridge model (Bursi et al., 2017). Since the selected case study structure is insensitive to broadband ground motions, the artificial ground motion model incorporates a pulse-like component (Dabaghi and Kiureghian, 2017), and it is calibrated against a set hazard-consistent site-specific real records. The framework is applied to compute the fragility analysis related to the lateral drift of one of the twelve piers of the Rio Torto Bridge.

This paper is organized as follows. Section 2 describes the proposed seismic fragility analysis framework. Section 3 introduces the Rio Torto Bridge case study. Section 4 describes both HF and LF structural simulators of the bridge. Section 5 describes the calibration of the artificial ground motion model using hazard-compatible site-specific seismic records. Section 6 summarizes the results of the seismic fragility analysis of the bridge. Section 7 includes limitations, future perspectives, and conclusions. For the sake of completeness, the entire machinery of surrogate modeling and, in particular, PCE-based GSA (Blatman and Sudret, 2011; Le Gratiet et al., 2017) and HK (Abdallah et al., 2019) are reported as appendices providing a self-consistent notation.

## 2 Seismic fragility analysis framework

### 2.1 Theoretical background

Let  $A(t)$  denote the stochastic process representing the input excitation of the system. The goal is to represent the process in terms of an aleatory component (i.e., the inherent variability of the process) and an epistemic component (i.e., the parametric variability of the process). Accordingly, it is convenient to express  $A(t)$  as follows.

$$A(t) = \mathcal{M}_a(t, \mathbf{Z}_a | \mathbf{X}_a), \quad (1)$$

where  $\mathcal{M}_a$  is a parametric stochastic model (or synthesis formula),  $\mathbf{Z}_a$  is a set of random variables representing the aleatory variability, and  $\mathbf{X}_a$  is a set of model parameters. In this setting, the model parameters are considered as random variables. However, this uncertainty is epistemic (i.e., can be reduced). Let  $Y$  denote the response QoI of a real system (e.g., the maximum displacement or internal force of a structural component), and  $\mathcal{M}_c(A(t), \mathbf{Z}_c | \mathbf{X}_c)$  a suitable (w.r.t. the QoI) stochastic structural simulator, where  $\mathbf{X}_c$  is a set of random model parameters and  $\mathbf{Z}_c$  is a set of random variables representing the aleatory variability of the structural model (e.g., the

inherent randomness of random fields in a stochastic finite element setting, (Stefanou, 2009)). It follows that  $Y$ , can be written as

$$Y = \mathcal{M}_c(\mathcal{M}_a(t, \mathbf{Z}_a | \mathbf{X}_a), \mathbf{Z}_c | \mathbf{X}_c), \quad (2)$$

$$= \mathcal{M}(\mathbf{Z} | \mathbf{X}), \quad (3)$$

where  $\mathcal{M} := \mathcal{M}_c \circ \mathcal{M}_a$ ,  $\mathbf{Z} = [\mathbf{Z}_a; \mathbf{Z}_c]$ , and  $\mathbf{X} = [\mathbf{X}_a; \mathbf{X}_c]$ . Observe that even when  $\mathcal{M}_c$  is a deterministic structural simulator—i.e.,  $\mathbf{Z}_c$  is not present— $\mathcal{M}$  is a stochastic simulator. In fact, in this case, given a realization of the model parameters,  $\mathbf{x}$ ,  $Y$  is still a random variable with aleatory uncertainty determined by the propagation of  $\mathbf{Z}_a | \mathbf{x}$ . Using Eq.3, the Cumulative Distribution Function (CDF) of  $Y$ , denoted by  $F_Y(y)$ , can be written as

$$F_Y(y) = \mathbb{P}(\mathcal{M}(\mathbf{Z} | \mathbf{X}) \leq y) = \int_{\mathbf{x}} \int_{\mathbf{z}} \mathbb{I}(\mathcal{M}(\mathbf{z} | \mathbf{x}) \leq y) dF_{\mathbf{Z}}(\mathbf{z}) dF_{\mathbf{X}}(\mathbf{x}), \quad (4)$$

where  $\mathbb{I}(\cdot)$  denotes the indicator function,  $\mathbb{P}(\cdot)$  denotes probability,  $F_{\mathbf{Z}}(\mathbf{z})$ ,  $F_{\mathbf{X}}(\mathbf{x})$  denote the joint CDFs, and  $dF_{\mathbf{Z}}(\mathbf{z}) = f_{\mathbf{Z}}(\mathbf{z})d\mathbf{z}$ ,  $dF_{\mathbf{X}}(\mathbf{x}) = f_{\mathbf{X}}(\mathbf{x})d\mathbf{x}$ , with  $f_{\mathbf{X}}(\mathbf{x})$  and  $f_{\mathbf{Z}}(\mathbf{z})$  being the joint probability densities. Observe that  $\mathbf{Z}$  is statistically independent of  $\mathbf{X}$ ; moreover,  $f_{\mathbf{X}}(\mathbf{x}) = f_{\mathbf{X}_c}(\mathbf{x}_c)f_{\mathbf{X}_a}(\mathbf{x}_a)$  under the (reasonable) assumption that the parameters of the seismic input and the structural simulator are statistically independent. Next, the conditional CDF of  $Y$  given a realization  $\mathbf{x}$  is simply

$$F_{Y|\mathbf{X}}(y|\mathbf{x}) = \mathbb{P}(\mathcal{M}(\mathbf{Z} | \mathbf{X} = \mathbf{x}) \leq y) = \int_{\mathbf{z}} \mathbb{I}(\mathcal{M}(\mathbf{z} | \mathbf{x}) \leq y) dF_{\mathbf{Z}}(\mathbf{z}). \quad (5)$$

Given the distribution function  $F_{Y|\mathbf{X}}$ , the  $p$ -quantile function returns the value  $y_p$  such that  $F_{Y|\mathbf{X}}(y_p|\mathbf{x}) = p$ . Assuming  $F_{Y|\mathbf{X}}$  is continuous and strictly monotonically increasing,  $y_p = F_{Y|\mathbf{X}}^{-1}(p|\mathbf{x})$ . However, since  $\mathbf{X}$  is a random variable,  $y_p$  is also a random variable and can be written as

$$Y_p = F_{Y|\mathbf{X}}^{-1}(p|\mathbf{X}) = \mathcal{M}_p(\mathbf{X}). \quad (6)$$

where, for convenience, we define  $\mathcal{M}_p(\cdot) := F_{Y|\mathbf{X}}^{-1}(p|\cdot)$ , and  $p \in [0, 1]$ . Therefore,  $Y_p$  can also be viewed as stochastic process indexed by  $p$ . Moreover,  $\mathcal{M}_p$  is a deterministic model, since the aleatory variability has been marginalized in Eq.6.

Given this general framework, a few observations need to be done for this specific study. First of all,  $A(t)$  is an artificial ground motion model, and  $\mathbf{X}_a$  is a physically meaningful set of ground motions parameters. Specifically, if the artificial ground motion model is a Gaussian filtered white noise, then  $\mathbf{Z}_a$  is a set of standard normal random variables (more details in Section 5). Second,  $\mathcal{M}_c$  is a deterministic structural simulator, where  $\mathbf{X}_c$  is the set of model parameters and  $\mathbf{Z}_c$  is not present. Finally, observe that despite its simplicity, Eq.6 involves a complex and highly non-trivial computational endeavor. In the following, this task is tackled using a non-intrusive UQ approach that assumes that  $\mathcal{M}_c$  (and therefore  $\mathcal{M}$ ) is a black-box solver.

## 2.2 Computational solution

In the context of earthquake engineering, the goal of this study is to determine the distribution of  $Y_p$  for different values of  $p$ . In general, the analytical solution of Eq.6 is not available; moreover, a classical Monte-Carlo-based solution is computationally prohibitive. In fact,  $\mathcal{M}_c$  is an "expensive" model and, therefore, also  $\mathcal{M}_p$ . A natural alternative to drastically reduce the computational cost is to replace the original model with a surrogate model. Let  $\hat{\mathcal{M}}_p$  denotes a surrogate model of  $\mathcal{M}_p$ , then

$$\hat{Y}_p = \hat{\mathcal{M}}_p(\mathbf{X}), \quad (7)$$

where  $\hat{Y}_p \approx Y_p$ . The statistics of  $\hat{Y}_p$  are then directly used for decision making. The surrogate model should be compatible with the artificial ground motion model, an HF *validated* structural simulator and the chosen QoI. Specifically, the proposed scheme builds on a combination of PCE-based GSA and HK, and it is here summarized in the following steps.

1. **Model definition and validation.** Define the QoI, a stochastic model of the input  $\mathcal{M}_a$  (Section 5), and a set of structural simulators  $\mathcal{M}_c$  (Section 4). In this study,  $c \in \{LF, HF\}$  where  $c = HF$  corresponds to the expensive-to-evaluate HF simulator whereas  $c = LF$  to a computationally cheaper LF simulator (Section 2.2 provides further detail on this choices). The definition of the models reflects the following criteria:
  - (a) The artificial ground motion model is defined w.r.t. a local seismic catalog based on an *existing* suitable ground motion selection (e.g., (Bradley, 2010; Iervolino et al., 2010; Baker, 2011)). In fact, this framework is designed to work complementary to any ground motion selection criteria, rather than to express a preference for a specific selection criterion or to propose a new one.
  - (b) The HF simulator successfully passed a comprehensive *validation* protocol. Validation entails a comparison of model predictions with physical experiments that adequately reproduce the real structural behavior (Trucano et al., 2006). This study uses HF simulators validated using HS. This minimizes the cost of conducting realistic structural testing campaigns compared to shake table testing (Schellenberg et al., 2009). To be robust to generalization error, the HF simulator incorporates an accurate description of the physics of the real structure, which includes geometric and material properties. Therefore, it is ranked first in terms of computational cost for a single evaluation amongst all structural simulators  $\mathcal{M}_c$ . As a result, the HF simulator is expected to succeed in representing the structural response with predetermined accuracy within a given validation domain.
  - (c) The LF simulator is a computationally cheaper proxy of its HF counterpart. For example, one could decide using different modeling paradigms for HF and LF simulators or 2D versus 3D geometrical representations. The main assumption of HK surrogate modeling is that the bias between LF and HF simulator responses is smoother than the HF simulator response (Ng and Eldred, 2012). Therefore, LF and HF simulator responses must be highly correlated. Hence, this study proposes to derive the LF simulator as a reduced-order representation of the HF simulator using dynamic substructuring (de Klerk et al., 2008). In particular, it is shown how to obtain a non-linear reduced-order model as an assembly of reduced-order linear components (Craig and Kurdila, 2006) connected by non-linear springs.
2. **Global-sensitivity-based dimensionality reduction.** Create a larger LF Experimental Design (ED)  $\{\mathcal{Y}_{LF,p}, \mathcal{X}\}$ , where  $\mathcal{Y}_{LF,p} = \{y_{LF,p}^{(1)}, \dots, y_{LF,p}^{(N_{LF})}\}$ ,  $\mathcal{X} = \{\mathbf{x}^{(1)}, \dots, \mathbf{x}^{(N_{LF})}\}$ ,  $\mathbf{x}^{(n)}$  is a generic sample of the input parameters, and  $y_{LF,p}^{(n)}$  is the corresponding LF estimate of the  $p$ -quantile of the QoI. Train a set of LF surrogates,  $\hat{\mathcal{M}}_{LF,p}^{PCE}(\mathbf{x})$ , based on  $\{\mathcal{Y}_{LF,p}, \mathcal{X}\}$  using PCE (Blatman and Sudret, 2011). Perform a PCE-based GSA (Le Gratiot et al., 2017) w.r.t. the QoI. Select and retain the input random variables that contribute most to the variability (variance) of the QoI and fix the remaining ones to their expected value. In practice, define  $\mathbf{X} = [\mathbf{X}_\alpha, \mathbf{x}_\beta]$ , where  $\mathbf{X}_\alpha$  are the "important random variables," and  $\mathbf{x}_\beta = E[\mathbf{X}_\beta]$  the rest of input parameters. A natural output of GSA are univariate effects of input parameters, which are the expectation of a QoI conditioned on the value of a single input variable (therefore, they provide information about the shape of the surrogate models). In this context they are used at step 4 for defining monotonic fragility models. A detailed summary on PCE-based GSA is reported in Appendix A.

3. **Hierarchical Kriging surrogate modeling.** Train a second smaller HF ED  $\{\mathbf{Y}_{HF,p}, \mathbf{X}_\alpha\}$ , where  $\mathbf{Y}_{HF,p} = \{y_{HF,p}^{(1)}, \dots, y_{HF,p}^{(N_{HF})}\}$ ,  $\mathbf{X}_\alpha = \{\mathbf{x}_\alpha^{(1)}, \dots, \mathbf{x}_\alpha^{(N_{HF})}\}$ ,  $\mathbf{x}_\alpha^{(n)}$  is a generic sample of the selected model parameters, and  $y_{HF,p}^{(n)}$  is the corresponding HF estimate of the  $p$ -quantile of the QoI. Train a set of MF surrogates  $\hat{\mathcal{M}}_{HF,p}^K(\mathbf{x}_\alpha)$  based on  $\{\mathbf{Y}_{HF,p}, \mathbf{X}_\alpha\}$  using HK. In this case, the PCE surrogate of the corresponding LF quantile is used as trend function (Han and Görtz, 2012; Abdallah et al., 2019). A short summary of HK surrogate modeling is reported in Appendix B.
4. **Probabilistic characterization of the QoI.** Compute the statistics of the QoI of interest (including fragility analysis) via Monte-Carlo-based UQ analysis using the HK surrogate model. Specifically, given an ordered sequence of quantiles  $\mathcal{P} = [p_1, \dots, p_n]$ , steps 2-3 can be implemented sequentially to obtain  $n$  maps (i.e., surrogate models) between  $\mathbf{Y}_{\mathcal{P}}$  and  $\mathbf{X}$ . Therefore, this  $n$  ordered sequence of surrogate models provides the complete discretized CDF of the QoI w.r.t. the input  $\mathbf{X} = \mathbf{x}$ , i.e.  $F(y_{\mathcal{P}}|\mathbf{x})$ . Observe that such description is sufficient for a fast inversion of Eq.6. Finally, fragility models of the QoI w.r.t. the important random variables ( $\mathbf{X}_\alpha$ ) are computed by MCS. Observe that not all the *marginal* fragility w.r.t. the single important variables are necessarily monotonous. Therefore, following the current practice, only the monotonic increasing fragilities are suitable for the PEER-PBEE framework. The univariate effects of QoI quantiles computed at step 2 guides this final selection.

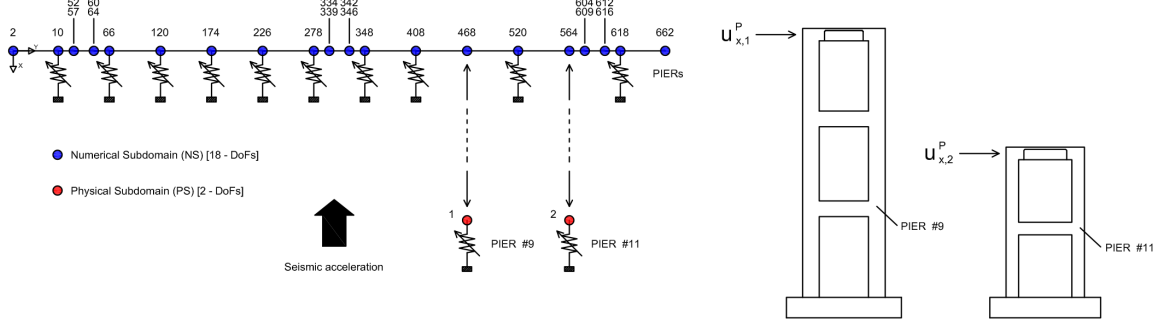
Despite the use of stochastic simulators (Eq.3), the outlined framework has the critical advantage of providing by construction (Eq.6) a—deterministic—map between the input parameters and a given quantile of the distribution of the QoI. The nature of the uncertainty associated with this distribution is aleatory. Specifically, it is the aleatory component,  $\mathbf{Z}$ , of the stochastic model,  $\mathcal{M}(\mathbf{Z}|\mathbf{x})$ . In fact, in the special case of a deterministic simulator any quantile will collapse into the deterministic solution of  $\mathcal{M}(\mathbf{x})$ . A cornerstone of the proposed framework is model calibration and validation with experimental data. In fact, the LF simulator can be characterized by an oversimplification of the real problem, phenomenological (and not validated) assumptions, and non-physical parameters. As a result, a rigorous global model validation becomes prohibitive, leading to not negligible model biases. On the other hand, the advantage of LF structural simulators lies in their reduced computational cost, enabling global studies. Few considerations need to be made in the context of earthquake engineering. In this case, an *EDP* of interest is the QoI; moreover, a vector of *IMs* is composed by either some of the "important" input parameters (i.e.,  $\mathbf{IM} \in \mathbf{X}_\alpha$ ) or by a set of instrumental IMs ( $\mathbf{IM} = [PGA, PGV, \dots]$ ). In the latter case, a statistical conversion (Suzuki and Iervolino, 2020) between the ground motion parameters and the instrumental IMs can be easily derived provided a large set of simulations. The proposed framework allows the computation of any statistic of interest for the selected *EDP*, including classical fragility functions and surfaces. In the fragility analysis context, a key passage of this framework is the GSA (step 2), which provides a rigorous selection of the important input parameters (i.e.,  $\mathbf{IM}$ ) w.r.t. to the *EDP* variability. Observe that this condition is explicitly dependent on the quantile of (major) interest. Therefore, it potentially eliminates the loss of correlation between  $\mathbf{IM}$  and *EDP* in the tail of fragility functions (Grigoriu, 2011) (if this probability region is of interest).

### 3 The Rio Torto Bridge case study

The Rio Torto Bridge is an RC structure built in the '70s and located on the motorway between Florence and Bologna, Italy. The bridge comprises two independent roadways of 400 m length and is characterized by a 13-span deck sustained by twelve piers. Three out of thirteen spans



(a)



(b)

Figure 1: The Rio Torto Bridge case study: a) side view retrieved from (Abbiati et al., 2015); b) hybrid model retrieved from (Bursi et al., 2017)

accommodate Gerber saddles, which protect the deck from restrained deformation due to pier settlement. Pier heights vary between a minimum of 13.80 m (Pier # 12) to a maximum of 41.00 m (Pier # 7). Figure 1b reports a schematic of the hybrid model of the Rio Torto Bridge. Non-linear springs represent the in-plane stiffness of numerical and physical piers activated by the lateral displacement of the deck. A schematic view of tested piers is also reported in Figure 1b. The Rio Torto Bridge was selected as a case study to investigate the seismic performance of old RC bridges and possible seismic retrofitting schemes within the framework of the RETRO project (Paolacci et al., 2014). The seismic response of the bridge was evaluated via HS. In detail, mock-up models of Pier #9 and #11 of 1:2.5 scale were built and tested via HS at ELSA Laboratory of the Joint Research Centre of Ispra, Italy. Figure 2a provides a picture of the entire installation at the JRC of Ispra while Figure 2b reports an overview of the finite-element model utilized to design the experiments.

The East-West and the North-South components of the Emilia earthquake of May 29, 2012, recorded from Mirandola station and downloaded from the ITACA database (Pacor et al., 2011) were considered as serviceability and ultimate limit state accelerograms (SLS and ULS, respectively). The response spectra of both SLS and ULS accelerograms are shown in Section 5 where the stochastic modeling of the seismic input for the fragility analysis is described. In this study, the epistemic uncertainty of the deterministic structural simulator parameters is considered negligible w.r.t. the ground motion parameters, therefore, we set  $\mathbf{X}_c = \bar{\mathbf{x}}_c^*$ . Therefore,  $\mathbf{X} \equiv \mathbf{X}_a$  and  $\mathbf{Z} \equiv \mathbf{Z}_a$ . For a comprehensive description of the HS campaign, the reader is addressed to (Abbiati et al., 2015; Bursi et al., 2017).

## 4 Computational modeling of the bridge

Two structural simulators of a single lane of the Rio Torto Bridge were implemented, namely, a HF finite-element and a LF state-space structural simulator. The former was initially implemented in OpenSees (McKenna et al., 2010) to support the design of the experimental campaign (see Figure

\*This corresponds to assign a delta Probability Density Function, i.e.,  $\delta(\mathbf{x}_c - \bar{\mathbf{x}}_c)$

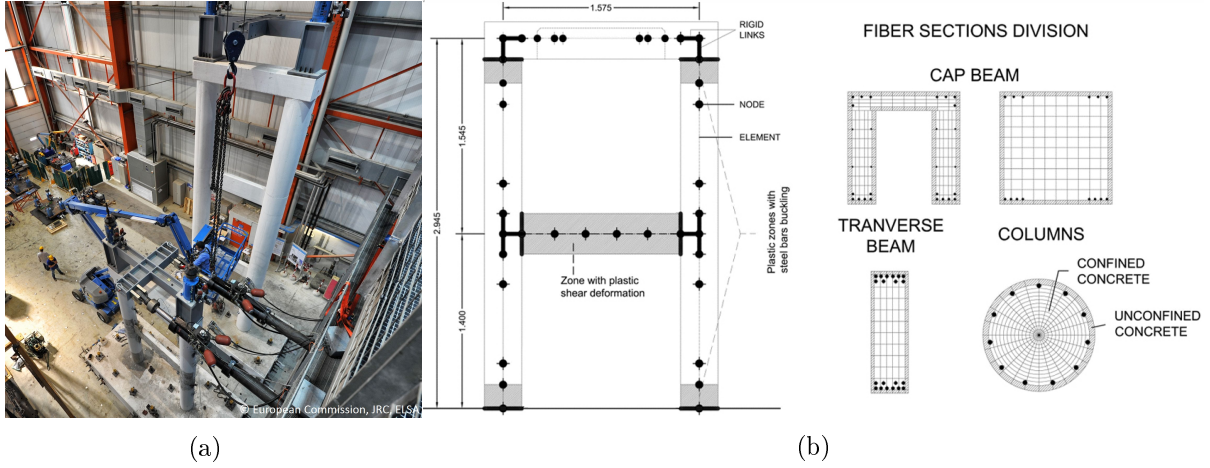


Figure 2: Tested piers: a) picture of the setup at JRC Ispra; b) finite-element model of Pier #11 implemented in OpenSees (McKenna et al., 2010)

2b, in this regard). The LF simulator was obtained, instead, via dynamic substructuring of the HF simulator. Accordingly, LF and HF structural simulators show almost the same response in the linear regime.

#### 4.1 High-fidelity finite-element model

The HF simulator was implemented in OpenSees (McKenna et al., 2010). Linear Bernoulli beam elements were used for the deck, whose response was assumed not to exceed the linear regime. Cylindrical hinges model Gerber saddles allowing for lateral and vertical rotations between deck elements while blocking relative torsional rotations. Displacement Degrees-of-Freedom (DoFs) of both abutments were constrained, but not rotations. A rigid link accounted for the offset distance between the cap beam axis and the center of gravity of the deck cross-section. Each pier was clamped at the base.

All piers were modeled using non-linear fiber-based elements thus discretizing longitudinal steel reinforcement of member cross-sections. The zero-tensile-strength *Concrete01* OpenSees material was adopted for concrete assuming a compressive strength  $f_{pc} = 11.47$  MPa and  $f_{pc} = 17.16$  MPa for piers characterized by solid and hollow cross-section columns, respectively. These values were calibrated based on the quasi-static response of Pier #9 and #11 obtained via HS. The *Steel02* OpenSees material was adopted for steel rebars assuming a tensile strength  $f_y = 360$  MPa. The *Pinching4* OpenSees material was used to model the hysteretic shear response of transverse beam elements. Parameter values were calibrated for a series of cyclic tests conducted on a 1/4 scale mock-up model of Pier #12 documented in (Paolacci and Giannini, 2012). Finally, a proportional Rayleigh damping model was adopted with mass multiplier  $\alpha_d = 0.27300$  and stiffness multiplier  $\beta_d = 0.00787$ . The vibration periods of the first four eigenmodes of the Rio Torto Bridge computed from the HF simulator are  $T = \{1.62, 1.55, 1.52, 0.88\}$  sec. Figure 3 compares the hysteretic loop of the lateral restoring force of Pier #11 obtained via HS (SLS and ULS accelerograms, *as built* configuration) to corresponding HF simulator predictions. As can be appreciated, the HF simulator effectively reproduces the lateral restoring force response of Pier #11. A single evaluation of the time history response of the HF simulator subjected to a 15 sec accelerogram sampled at 1 msec takes about 600 sec on a standard laptop equipped with an Intel 1.80 GHz i7-8565U CPU and 16 GB RAM or similar. For a more detailed description of the HF simulator, the reader should refer to (Abbiati et al., 2015).

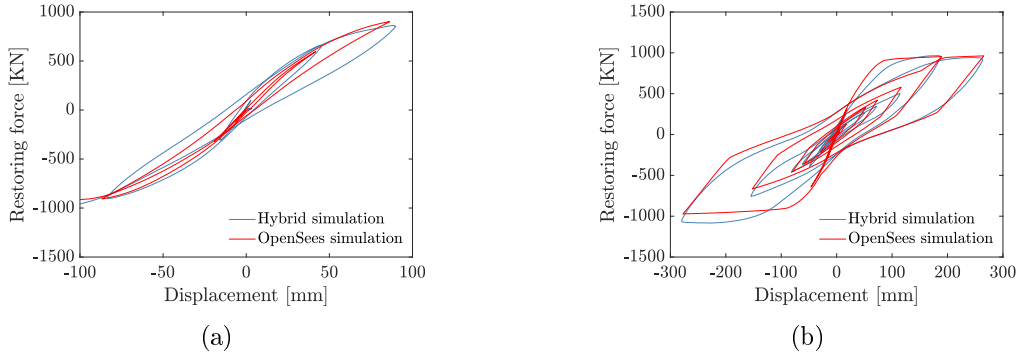


Figure 3: Measured and simulated hysteresis loops of the lateral restoring force of Pier #11: a) SLS; b) ULS.

## 4.2 Low-fidelity state-space model

A linearized version of the HF simulator supported the computation of reduced-order mass and stiffness matrices of deck and piers of the LF simulator via component-mode synthesis (Craig and Kurdila, 2006), which is a specific dynamic substructuring method (de Klerk et al., 2008). In detail, the reduced-order model of the deck was obtained via static condensation retaining only lateral displacement DoFs of piers and Gerber saddles,

$$\begin{cases} \dot{\mathbf{u}} = \mathbf{v} \\ \dot{\mathbf{v}} = \mathbf{m}^{-1} (\mathbf{l} \cdot \mathbf{r} - \mathbf{c} \cdot \mathbf{v} - \mathbf{k} \cdot \mathbf{u} - \mathbf{t} \cdot a_g(t)), \end{cases} \quad (8)$$

where  $\mathbf{u}$  and  $\mathbf{v}$  are the 18 retained displacement and velocity DoFs, respectively;  $\mathbf{k}$ ,  $\mathbf{c}$  and  $\mathbf{m}$  are reduced-order stiffness, damping and mass matrices, respectively, whereas  $\mathbf{t}$  is the seismic mass vector. The latter multiplies the seismic accelerogram  $a_g(t)$  to obtain the seismic loading. The  $18 \times 12$  Boolean matrix  $\mathbf{l}$  collocates the 12 pier restoring forces stored in  $\mathbf{r} = \{r_1, \dots, r_{12}\}$  to the related state-space equation. A non-linear single-DoF system based on a Bouc-Wen restoring force was calibrated to mimic the response of the corresponding pier in the HS structural simulator,

$$\begin{cases} \dot{u}_i = v_i \\ \dot{v}_i = m_i^{-1} [g_i(t) - c_i v_i - r_i - t_i a_g(t)] \\ \dot{r}_i = [A_i + (\beta_i \text{sign}(r_i v_i) - \gamma_i) |r_i|^n] v_i, \end{cases} \quad (9)$$

where  $u_i$ ,  $v_i$ , and  $r_i$  are the three state variables, namely, displacement, velocity, and hysteretic restoring force, whereas  $g_i(t)$  represent the deck reaction force of the  $i$ -th pier. Mass  $m_i$  and seismic mass  $t_i$  were obtained via static condensation as well. For each pier, the top lateral displacement DoF was retained as master DoF, whereas the others were condensed. Consistently with the HF simulator, viscous damping  $c_i$  was computed assuming a proportional Rayleigh damping with mass multiplier  $\alpha_d = 0.27300$  and stiffness multiplier  $\beta_d = 0.00787$ . The parameters  $A$ ,  $\beta$ ,  $\gamma$  and  $n$  refer to the Bouc-Wen model (Ikhouane and Rodellar, 2007), which describes the evolution of the hysteretic restoring force  $r_i$ . As analogously done for damping, mass, and seismic mass, the parameter  $A$ , which represents the initial stiffness of the non-linear spring, was obtained via static condensation of the HF pier model. On the other hand,  $n$  was assumed constant and equal to one, whereas  $\beta$  and  $\gamma$  were calibrated to match the static response of the corresponding OpenSees pier model subjected to ten sinusoidal displacement cycles producing 0.5 % drift. Figure 4 compares the dynamic response of Pier #11 obtained from time history analyses of LF and HF structural simulators considering the ULS accelerogram of the HS campaign described in Section 3. A single evaluation of the time history response of the LF simulator subjected to a 15 sec accelerogram sampled at 1 msec takes about 20 sec on a standard laptop equipped with an Intel 1.80 GHz i7-8565U CPU and 16 GB RAM.

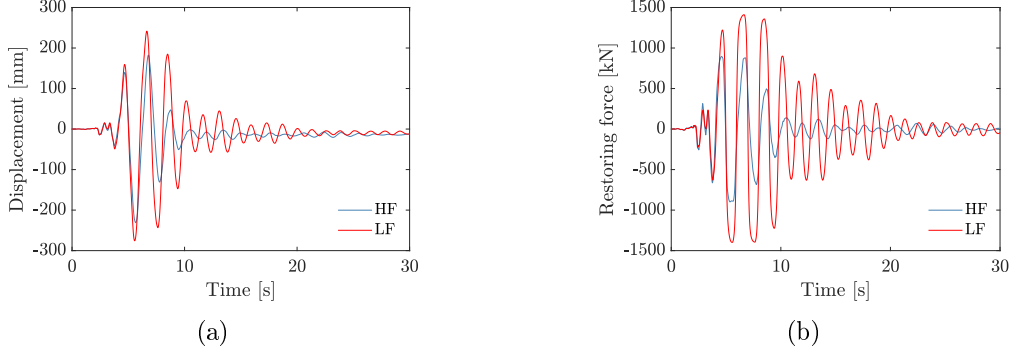


Figure 4: LF and HF simulations of the seismic response of Pier #11: a) displacement, b) restoring force.

## 5 Stochastic modeling of the seismic input

The lateral motion of the Rio Torto Bridge is characterized by a relatively long period of vibration. Consequently, its reliability is not strongly affected by broadband motions. On the contrary, it is vulnerable to pulse like motions with frequencies close to the structural ones. Generally, the presence of a strong pulse component is more likely in near field motions. As a consequence, this study employs the stochastic model proposed by Dabaghi and Der Kiureghian (Dabaghi and Kiureghian, 2017), which is designed for such type of excitations.

The model is composed by a residual broad-band process (as done in (Rezaeian and Der Kiureghian, 2008)), and a modified version of the Mavroeidis, pulse model with random parameters (Mavroeidis, 2003),

$$\begin{aligned}
 V_{pul}(t) &= \mathcal{M}_{pul}(t, \mathbf{X}_{pul}) \\
 &= \left\{ \frac{1}{2} V_p \cos \left[ 2\pi \left( \frac{t - T_{max,p}}{T_p} \right) + \nu \right] - \frac{D_r}{\gamma T_p} \right\} \left\{ 1 + \cos \left[ \frac{2\pi}{\gamma} \left( \frac{t - T_{max,p}}{T_p} \right) \right] \right\}, \quad (10) \\
 t_{i,p} &< t \leq t_{f,p}.
 \end{aligned}$$

where  $\mathbf{X}_{pul} = [V_p, T_p, T_{max,p}, \gamma, \nu]$ . Specifically,  $V_p$  and  $T_p$  are pulse amplitude and period, respectively,  $\gamma$  represents the number of oscillations within the pulse,  $\nu$  is the phase angle shift w.r.t. the time modulation function, and  $T_{max,p}$  is a location parameter for the peak of the excitation.  $D_r$  has been introduced in (Dabaghi and Kiureghian, 2017) to guarantee zero residual displacement at the end of the excitation, and it is defined as

$$D_r = V_p T_p \frac{\sin(\nu + \gamma\pi) - \sin(\nu - \gamma\pi)}{4\pi(1 - \gamma^2)}. \quad (11)$$

Finally,  $t_{i,p} = T_{max,p} - 0.5\gamma T_p$ , and  $t_{f,p} = T_{max,p} + 0.5\gamma T_p$  represent the start and the end of the pulse motion. While the pulse is modeled in the velocity domain, the residual is modeled in the acceleration domain, i.e.,  $a_{res}(t) = a(t) - \dot{v}_{pul}(t)^*$ . Since the residual of the acceleration is a broadband motion, the model follows the same principles of (Rezaeian and Der Kiureghian, 2008), i.e.,

$$A_{res}(t) = \mathcal{M}_{res}(t, \mathbf{Z} | \mathbf{X}_{res}) = q(t | \mathbf{X}_q) \frac{h(t | \mathbf{X}_h) * W(t, \mathbf{Z})}{\sigma_h(t, \mathbf{Z} | \mathbf{X}_h)}, \quad (12)$$

where  $*$  denotes time convolution;  $\mathbf{X}_{res} = [\mathbf{X}_q, \mathbf{X}_h]$ ;  $q(t | \mathbf{X}_q)$  is a parametric time modulating function with random parameters  $\mathbf{X}_q$ ;  $h(t | \mathbf{X}_h)$  is the impulse-response function of a linear filter

\*lower case letters are used to indicate the single excitation; moreover, notice the time derivative on the pulse component.

with time varying random parameters, where  $\mathbf{X}_h$  represents a set of time invariant parameters;  $W(t, \mathbf{Z}) = \sum_n^{N_t} \delta(t - t_n) Z_n$  is a band-limited white noise process, where  $\mathbf{Z} = [Z_1, \dots, Z_{N_t}]$  is a standard normal vector; and  $\sigma_h(t, \mathbf{Z} | \mathbf{X}_h)$  is the variance of the convoluted process (i.e., the numerator of Eq.12). The modulating function proposed in (Dabaghi and Kiureghian, 2017) for near-field motions is

$$q(t | \mathbf{X}_q) = \begin{cases} C \left( \frac{t}{T_{max,q}} \right)^\alpha, & 0 < t \leq t_{max,q} \\ C \exp[-\beta(t - T_{max,q})], & t_{max,q} < t, \end{cases} \quad (13)$$

where  $\mathbf{X}_q = [\alpha, \beta, C, T_{max,q}]$  are the parameters of the function. Specifically,  $\alpha$  and  $\beta$  are shape parameters controlling the ramping and decreasing phase of the residual,  $C$  is a scale factor, and  $T_{max,q}$  is a location parameter defining the peak of the residual excitation. Moreover, it can be shown that a one-to-one mapping exists between these parameters and  $D_{5-95, I_{a,res}} = T_{95, I_{a,res}} - T_{5, I_{a,res}}$ ,  $T_{30, I_{a,res}}$ , and  $I_{a,res}$ —where  $T_{p, I_{a,res}}$  is the time corresponding to the  $p$  % of the cumulative Arias intensity of the residual,  $I_{a,res}$ . It follows that  $\mathbf{X}_q$  can be written as  $\mathbf{X}_q = [I_{a,res}, T_{30, I_{a,res}}, D_{5-95, I_{a,res}}]$ . The filter is defined by

$$h(t | \mathbf{X}_h) = \frac{\omega_f(t)}{\sqrt{1 - \zeta_f^2}} \exp[-\omega_f(t) \zeta_f \cdot t] \sin \left[ \omega_f(t) \sqrt{1 - \zeta_f^2} \cdot t \right]. \quad (14)$$

In Eq.14, the main frequency,  $\omega_f(t)$ , is evolving linearly with time. Specifically,  $\omega_f(t) = \omega_{mid} + \dot{\omega}(t - T_{30, I_a})$ , where  $\omega_{mid}$  is the frequency at time  $T_{30, I_a}$  (i.e., at 30 % of the cumulative Arias intensity of the residual) and  $\dot{\omega}$  is the rate of change of the frequency with time. The damping of the filter,  $\zeta_f$ , is considered time invariant. It follows that  $\mathbf{X}_h = [\omega_{mid}, \dot{\omega}, \zeta]$ . For further details the reader should refer to (Dabaghi and Kiureghian, 2017). Finally, the artificial ground motion model can be written as

$$A(t) = \mathcal{M}_a(t, \mathbf{Z} | \mathbf{X}_a) = \mathcal{M}_{res}(t, \mathbf{Z} | \mathbf{X}_{res}) + \dot{\mathcal{M}}_{pul}(t, \mathbf{X}_{pul}) = A_{res}(t) + \dot{V}_{pul}(t), \quad (15)$$

where  $\mathbf{X}_a = [\mathbf{X}_{res}, \mathbf{X}_{pul}]$ .

In order to find parameter ranges consistent with the seismic hazard characteristic of the site, the artificial ground motion model was calibrated against real seismic records following the procedure explained in (Dabaghi and Kiureghian, 2017). In detail, the seismic records of real events were selected based on the disaggregation analysis of the PGA with probability of exceedance of 2 % in 50 years (Bazzurro and Allin Cornell, 1999) reported in a previous work of the last author (Alessandri et al., 2013)\*. Then, it was found that only pulse-like ground motions were likely to cause damage to the structure. Consequently, only pulse-like motions were retained and used for the calibration of the artificial ground motion model. It follows that the analysis of this case study focuses on pulse-like excitations. Table 1 reports the list of the 16 selected records, whose corresponding accelerograms were downloaded from the ITACA database (Pacor et al., 2011). All records belong to the Emilia earthquake occurred on May 29, 2012 (Italy). Each of the 16 records listed in Table 1 comprise N-S and E-W acceleration records, which were decomposed into principal components as explained in (Baker, 2007). Velocity pulses were found on 12 over  $16 \times 2$  components only, which were retained for the calibration. Figure 5 reports displacement, velocity and acceleration response spectra of the 12 retained components as well as the response spectra of the SLS and ULS accelerograms used for the RETRO experimental campaign. The response spectra of the selected records, which correspond to the gray lines, fall within the range established by the response spectra of SLS and ULS accelerograms adopted during experiments and, therefore, utilized to calibrate the HF simulator of the Rio Torto Bridge. The artificial

---

\*In principle, peak ground velocity is a more suited intensity measure for structures characterized by long vibration periods such as the Rio Torto Bridge. However, the fragility analysis reported in (Alessandri et al., 2013) shows that PGA well correlates with pier drift for this specific case.

Table 1: Selected records associated with the Emilia earthquake of May 29, 2012 (Italy).

| Event ID     | Time [h:m:s] | $M_W$ | $D$ [km] | Station code | Latitude [deg] | Longitude [deg] |
|--------------|--------------|-------|----------|--------------|----------------|-----------------|
| IT-2012-0011 | 07:00:02     | 6     | 4.1      | MRN          | 44.878231      | 11.061743       |
| IT-2012-0011 | 07:00:02     | 6     | 4.1      | MIRE         | 44.878212      | 11.061747       |
| IT-2012-0011 | 07:00:02     | 6     | 9.3      | T0814        | 44.793300      | 10.969200       |
| IT-2012-0011 | 07:00:02     | 6     | 4.5      | MIRH         | 44.882400      | 11.063100       |
| IT-2012-0011 | 07:00:02     | 6     | 5.1      | MIR02        | 44.886948      | 11.073198       |
| IT-2012-0011 | 07:00:02     | 6     | 0.5      | MIR01        | 44.844042      | 11.071316       |
| IT-2012-0011 | 07:00:02     | 6     | 11.2     | MIR03        | 44.938400      | 11.104500       |
| IT-2012-0011 | 07:00:02     | 6     | 13       | MIR04        | 44.927433      | 11.178312       |
| IT-2012-0010 | 10:55:56     | 5.5   | 6.8      | T0819        | 44.887300      | 10.898700       |
| IT-2012-0011 | 07:00:02     | 6     | 11.3     | T0813        | 44.877800      | 11.199200       |
| IT-2012-0011 | 07:00:02     | 6     | 14.4     | T0800        | 44.848600      | 11.247900       |
| IT-2012-0011 | 07:00:02     | 6     | 6.1      | SAN0         | 44.838000      | 11.143000       |
| IT-2012-0011 | 07:00:02     | 6     | 8.6      | MIR08        | 44.916900      | 11.089500       |
| IT-2012-0011 | 07:00:02     | 6     | 9.9      | T0802        | 44.875000      | 11.181600       |
| IT-2012-0011 | 07:00:02     | 6     | 10.7     | T0818        | 44.934800      | 11.030400       |
| IT-2012-0011 | 07:00:02     | 6     | 14.3     | T0811        | 44.783800      | 11.226500       |

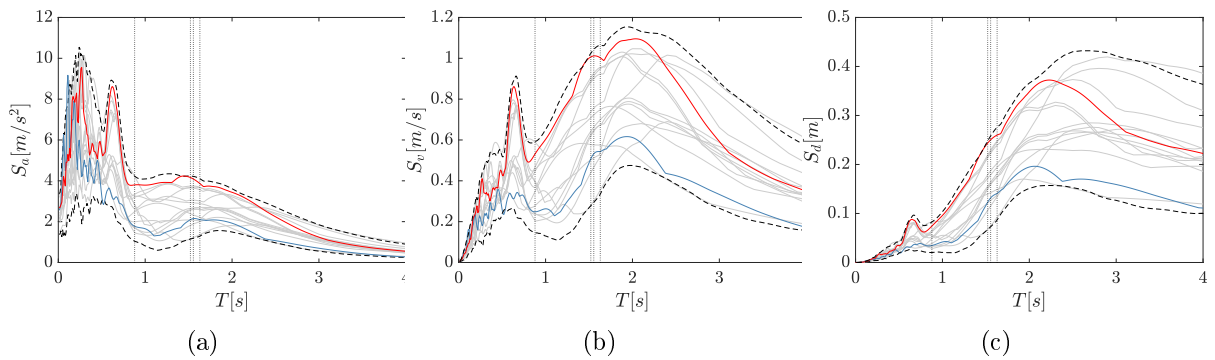


Figure 5: Selected records with pulse-like components: a) acceleration; b) velocity; c) displacement response spectra. Grey lines refer to single retained records with pulse-like component whereas black dashed lines indicate the corresponding 95 % confidence interval. Blue and red lines indicate SLS and ULS records used for the HS campaign, respectively. The periods of the first four eigenmodes of the Rio Torto Bridge estimated with the HF simulator are also reported.

Table 2: Parameters of Dabaghi and Der Kiureghian’s model identified on the pulse-like motions. Average values  $\mu$ , standard deviations  $\sigma$ , and coefficients of variations  $CoV$  and min and max bounds are computed over the 12 selected records.

| Record   | $V_p$ | $T_p$ | $\gamma$ | $\nu$ | $t_{max,p}$ | $I_{a,res}$ | $T_{30,I_{a,res}}$ | $D_{5-95,I_{a,res}}$ | $\omega_{mid}$ | $\dot{\omega}$ | $\zeta$ |
|----------|-------|-------|----------|-------|-------------|-------------|--------------------|----------------------|----------------|----------------|---------|
| 1        | 0.282 | 2.094 | 2.906    | 1.272 | 2.739       | 1.029       | 2.040              | 7.095                | 29.327         | 0.823          | 0.338   |
| 2        | 0.282 | 2.197 | 2.348    | 3.262 | 2.133       | 0.777       | 2.260              | 7.490                | 33.884         | 0.950          | 0.444   |
| 3        | 0.292 | 2.072 | 2.893    | 1.302 | 2.546       | 0.932       | 1.975              | 7.020                | 25.006         | 0.493          | 0.304   |
| 4        | 0.276 | 2.139 | 2.434    | 3.327 | 1.947       | 0.619       | 2.105              | 7.115                | 23.464         | 1.264          | 0.405   |
| 5        | 0.303 | 2.334 | 2.831    | 1.409 | 2.615       | 0.515       | 2.070              | 7.040                | 20.953         | 0.472          | 0.423   |
| 6        | 0.249 | 2.394 | 2.491    | 2.985 | 1.834       | 0.297       | 2.055              | 7.465                | 19.566         | 1.368          | 0.579   |
| 7        | 0.363 | 2.602 | 2.449    | 3.507 | 2.580       | 0.897       | 2.270              | 7.265                | 39.586         | 0.135          | 0.585   |
| 8        | 0.196 | 2.425 | 2.917    | 1.687 | 3.251       | 0.716       | 2.385              | 7.890                | 43.533         | -0.344         | 0.462   |
| 9        | 0.392 | 2.282 | 2.350    | 4.530 | 2.862       | 0.881       | 2.305              | 7.185                | 32.215         | 0.212          | 0.306   |
| 10       | 0.292 | 1.949 | 2.339    | 2.616 | 1.472       | 0.408       | 1.530              | 4.195                | 23.015         | 1.948          | 0.408   |
| 11       | 0.218 | 1.762 | 2.418    | 3.069 | 1.748       | 0.335       | 1.390              | 3.115                | 33.868         | 0.949          | 0.378   |
| 12       | 0.205 | 2.688 | 2.212    | 1.924 | 3.352       | 0.298       | 2.025              | 6.720                | 30.052         | -0.875         | 0.349   |
| min      | 0.196 | 1.762 | 2.212    | 1.272 | 1.472       | 0.297       | 1.390              | 3.115                | 19.566         | -0.875         | 0.304   |
| max      | 0.392 | 2.688 | 2.917    | 4.530 | 3.352       | 1.029       | 2.385              | 7.890                | 43.533         | 1.948          | 0.585   |
| $\mu$    | 0.279 | 2.245 | 2.549    | 2.574 | 2.423       | 0.642       | 2.034              | 6.633                | 29.539         | 0.616          | 0.415   |
| $\sigma$ | 0.056 | 0.254 | 0.249    | 1.001 | 0.573       | 0.255       | 0.286              | 1.378                | 7.159          | 0.742          | 0.089   |
| $CoV$    | 0.201 | 0.113 | 0.098    | 0.389 | 0.236       | 0.398       | 0.141              | 0.208                | 0.242          | 1.203          | 0.214   |

ground motion model with pulse-like motion was calibrated for each of the 12 retained records following the procedure described in (Dabaghi and Kiureghian, 2017). The parameter estimates are reported in Table 2. Noteworthy, correlation between each pair of ground motion model parameters was small and therefore neglected in the following. However, if relevant, parameter correlation can be recovered when sampling fragility models (e.g., using copulas (Torre et al., 2019b)). Figure 6 compares 50 realizations of artificial records to the reference real record (with parameters listed in the second entry of Table 2).

## 6 Seismic fragility analysis of the bridge

The most critical nonlinearity characterizing the structural response of the bridge is associated with shear failure of transverse beams of piers. Such structural elements are characterized by poor shear reinforcement and thus prone to brittle failure. This damage mechanism is activated by in-plane lateral deflection of the pier and, therefore, highly correlated with drift (Alessandri et al., 2013). Accordingly, lateral drift peak of piers was selected as QoI/EDP for fragility models. Consistently with the notation introduced in the previous sections, input variables and QoIs of for the fragility analysis read,

$$\mathbf{Y} = \{u_1, \dots, u_{12}\}, \mathbf{X} \equiv \mathbf{X}_a = \{V_p, T_p, \gamma, \nu, T_{max,p}, I_{a,res}, T_{30,I_{a,res}}, D_{5-95,I_{a,res}}, \omega_{mid}, \zeta\} \quad (16)$$

where  $u_i$  represents the lateral drift peak of pier  $i$ -th. However, due to space limitation, only the results related to the lateral drift peak of Pier #11, which is referred to as response QoI hereinafter, are reported and discussed.

A GSA of the QoI was performed to retain only the relevant parameters of the artificial ground motion model. Since GSA is used to uncover the inner workings of the LF simulator, in this stage, it is legitimate to assume that all input variables are independently distributed. For

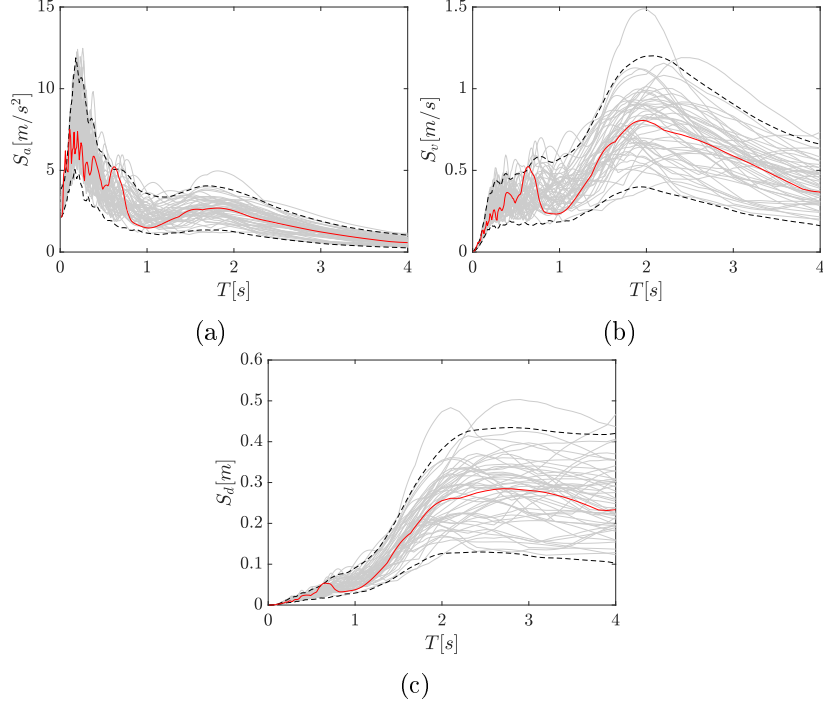


Figure 6: Response spectra of 50 realizations of the artificial ground motion model calibrated against the second record of Table 2: a) acceleration; b) velocity; c) displacement response spectra. Red lines refer to the reference record, grey lines represent the 50 realizations of the artificial ground motion model, and black dashed lines indicate the corresponding 95 % confidence interval.

a given sample  $\mathbf{X} = \mathbf{x}$ , 100 realizations of  $\mathbf{Z}$  were found to be sufficient to provide stable estimates of the QoI quantiles. Noteworthy, the same number of realizations was adopted in the work of [Gidaris et al. \(2015\)](#) to estimate mean and variance of the QoIs prior to surrogate modeling. According to step 2 of the proposed framework, a large LF ED was evaluated for 200 samples of  $\mathbf{X}$  considering the quantiles  $\mathcal{P} = \{0.05 : 0.05 : 0.95\}$ . Given that the computational cost of the LF simulator was 20 sec/run, the computational cost of the LF ED was  $20 \times 200 \times 100 = 400,000$  sec (about 4.6 days). The corresponding PCE-based total Sobol' indices are reported in Table 3 for the response QoI quantiles  $\mathcal{P} = \{0.1 : 0.1 : 0.9\}$  only. In this regard, the leave-one-out errors  $\epsilon_{loo}$  highlight fairly accurate PCEs (similar errors were obtained up to 0.99 quantiles for all piers). For all quantiles, the contribution of  $V_p$ ,  $T_p$ ,  $I_{a,res}$ ,  $\omega_{mid}$  and  $\zeta$  to the variability of the QoI is dominant. The same result was observed for all the other piers. Accordingly, constant average values reported in Table 2 were set for all other parameters in the following MF surrogate modeling stage. Among retained parameters, univariate effects spot monotonic increasing relationships with the response QoI for  $V_p$ ,  $I_{a,res}$  and  $\zeta$ . In this regard, Figure 7 reports the univariate effects of these parameters obtained from the LF surrogate model. Accordingly,  $V_p$  and  $I_{a,res}$  were employed as IMs for computing the fragility models.

Following step 3 of the framework, a small HF ED of 10 samples was evaluated using the HF simulator of the bridge considering,

$$\mathbf{X}_\alpha = \{V_p, T_p, I_{a,res}, \omega_{mid}, \zeta\}, \quad (17)$$

$$\mathbf{x}_\beta = E \left[ \{\gamma, \nu, T_{max,p}, T_{30,I_{a,res}}, D_{5-95,I_{a,res}}, \omega_{mid}\} \right]. \quad (18)$$

For each sample of the HF ED, estimates of response QoI quantiles were computed considering 100 realizations of the ground motion model. Given that the computational cost of the HF simulator was about 600 sec/run, the computational cost of the HF ED was about  $600 \times 10 \times 100 =$

Table 3: PCE-based total Sobol' indices of the response QoI (drift peak of Pier #11).

| $\mathcal{P}$ | $\epsilon_{loo}$ | $V_p$ | $T_p$ | $\gamma$ | $\nu$ | $t_{max,p}$ | $I_{a,res}$ | $T_{30,I_{a,res}}$ | $D_{5-95,I_{a,res}}$ | $\omega_{mid}$ | $\zeta$ |
|---------------|------------------|-------|-------|----------|-------|-------------|-------------|--------------------|----------------------|----------------|---------|
| 0.100         | 0.035            | 0.548 | 0.463 | 0.026    | 0.002 | 0.001       | 0.012       | 0.003              | 0.001                | 0.008          | 0.008   |
| 0.200         | 0.023            | 0.553 | 0.428 | 0.032    | 0.004 | 0.002       | 0.013       | 0.001              | 0.006                | 0.010          | 0.005   |
| 0.300         | 0.020            | 0.554 | 0.415 | 0.030    | 0.003 | 0.002       | 0.020       | 0.001              | 0.005                | 0.011          | 0.005   |
| 0.400         | 0.018            | 0.551 | 0.404 | 0.024    | 0.008 | 0.000       | 0.025       | 0.006              | 0.004                | 0.020          | 0.010   |
| 0.500         | 0.019            | 0.545 | 0.390 | 0.028    | 0.004 | 0.002       | 0.036       | 0.002              | 0.003                | 0.021          | 0.012   |
| 0.600         | 0.022            | 0.562 | 0.356 | 0.025    | 0.001 | 0.002       | 0.051       | 0.001              | 0.002                | 0.025          | 0.016   |
| 0.700         | 0.017            | 0.560 | 0.325 | 0.025    | 0.001 | 0.003       | 0.065       | 0.002              | 0.005                | 0.036          | 0.021   |
| 0.800         | 0.029            | 0.547 | 0.284 | 0.022    | 0.001 | 0.003       | 0.092       | 0.002              | 0.008                | 0.047          | 0.031   |
| 0.900         | 0.040            | 0.522 | 0.222 | 0.025    | 0.004 | 0.006       | 0.132       | 0.004              | 0.015                | 0.064          | 0.047   |

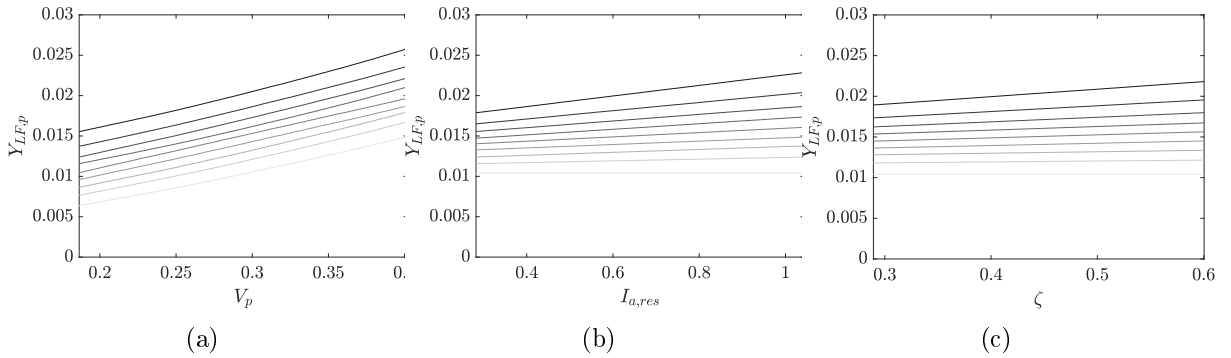


Figure 7: Univariate effects for the response QoI (drift peak of Pier #11) for the quantiles  $\mathcal{P} = \{0.1 : 0.1 : 0.9\}$ . Lighter curves refer to quantile  $p = 0.1$  while darker curves refer to quantile  $p = 0.9$ .

600,000 sec (about 7 days).

The main assumption of HK surrogate modeling is that the bias between LF and HF simulator responses is smoother than the HF simulator response (Ng and Eldred, 2012). Therefore, instead of absolute accuracy, the only requirement for the LF simulator response is to be highly correlated with the HF simulator response. The correlation plots of Figure 8 demonstrates that LF and HF simulators satisfy such requirement.

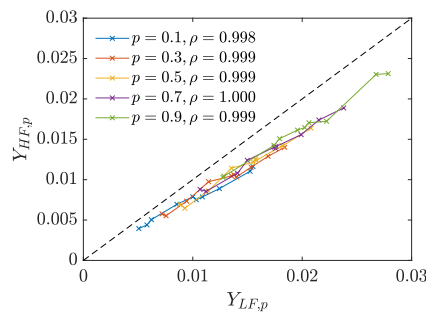


Figure 8: Correlation between LF and HF response quantiles (drift peak of Pier #11) on the HF ED samples  $\mathcal{X}_\alpha$ .

Following step 3 of the framework, a MF surrogate model of the QoI was computed using HK. The LF surrogate model computed at step 2 was used as trend function. Accordingly, MF- $n$  indicates the MF surrogate model (and the corresponding fragility model) computed with  $n$  samples of the HF ED. In all cases, a Matérn 5/2 correlation function  $R(\mathbf{X} - \mathbf{X}'|\boldsymbol{\theta})$  was

adopted. Since PCE is a powerful denoiser (see Torre *et al.* (Torre *et al.*, 2019a)), the LF surrogate can be trained on *noisy* estimates of the QoI quantiles based on a smaller number of samples of  $\mathbf{Z}$  resulting in a substantial reduction of computational cost for the LF ED. To support this statement, an additional set of MF surrogate models (and the corresponding fragility model) was computed considering LF surrogates trained on noisy QoI estimates obtained with 20 ground motion realizations.

Following step 4 of the framework, the fragility models reported in Figure 9 were computed via Monte-Carlo-based UQ forward analysis of MF surrogate models using  $V_p$  and  $I_{a,res}$  as IMs. These IMs are associated with the two largest total Sobol' indices (Table 3) and provided with an average monotonic relationship with the QoI/EDP (Figure 7). Specifically, Figures 9a-b-c refer to the fragility model based on a LF surrogate model trained with QoI quantile estimates obtained with 100 ground motion realizations. Similarly, Figures 9d-e-f refer to the fragility model based on a LF surrogate model trained with QoI quantile estimates obtained with 20 ground motion realizations. Both fragility models consider a threshold value  $\bar{y} = 0.01$  for the QoI/EDP (Pier #11 drift peak), which is associated with onset of concrete cover spalling and crack opening in transverse beams (Alessandri *et al.*, 2013). As can be appreciated from Figure 9, the two fragility models show a quite good agreement, demonstrating that noisy LF quantile estimates computed with 20 ground motion realizations are sufficiently accurate to support the following MF surrogate modeling stage.

In order to demonstrate the accuracy of the proposed methodology, both fragility models are compared to crude Monte Carlo estimates of the failure probability of the HF simulator. In detail, nine validation points were obtained as Cartesian product between  $V_p = \{0.2, 0.3, 0.4\}$  and  $I_{a,res} = \{0.4, 0.6, 1.0\}$ . In this regard, the red diamonds of Figure 9 indicate mean value and 95 % confidence interval of each failure probability estimate obtained with 100 samples of the HF simulator response <sup>†</sup>—i.e., circa 600,000 sec (about 7 days) per point of computational time. For the sake of clarity, for each fragility model, two orthogonal sections intersecting the mid validation point ( $V_p = 0.3$  and  $I_{a,res} = 0.6$ ) are also included in Figure 9. The 95 % confidence interval of the MF-10 fragility model is also reported as red-shaded area. Besides the sections of the MF-10 fragility model and its 95 % confidence interval, three additional fragility models are compared, namely LF, MF-8 and MF-9. As can be observed, fragility models computed from the LF surrogate are highly biased whereas fragility models computed from MF-8 and MF-9 surrogates are almost indistinguishable from MF-10.

For both fragility models the cost for the HF ED was about 600,000 sec of computation (about 7 days). However, the cost for the LF ED considerably dropped from 400,000 to 80,000 sec of computation (from about 4.6 to 0.9 days) by reducing the number of ground motion realizations utilized for quantile estimation from 100 to 20. As a matter of comparison, the total cost for the nine validation points obtained via MCS of the HF simulator was about 5,400,000 sec of computation (circa 63 days).

Although both LF and MF surrogate models were computed assuming independent uniformly distributed ground motion parameters, fragility models can be easily re-sampled considering a joint PDF calibrated for the specific seismic hazard. Also, provided with such simulation framework, ground motion parameters can be mapped to instrumental IMs as illustrated in (Suzuki and Iervolino, 2020).

---

<sup>†</sup>Notice that with 100 simulations the mean estimate is stable, while the confidence bounds should be considered as indicative.

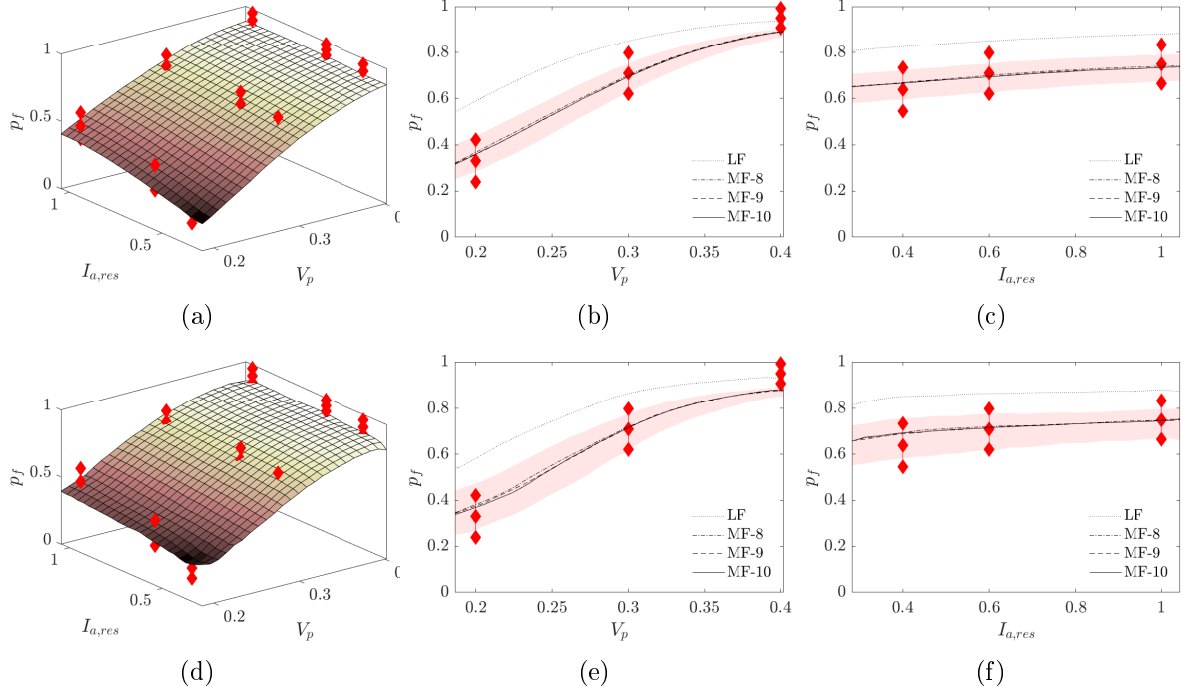


Figure 9: Fragility models and related mid sections along  $V_p$  and  $I_{a,res}$  computed for a lateral drift threshold of 1%. Underlying LF surrogates trained with response quantiles obtained from 100 (a-b-c) and 20 (d-e-f) ground motion realizations.

## 7 Conclusions

This study introduced a computational framework for efficient and accurate seismic fragility analysis based on a combination of artificial ground motions and surrogate modeling of multiple stochastic simulators characterized by different levels of fidelity. The effectiveness of the proposed framework is demonstrated throughout a benchmark case study, which consists of a reinforced concrete bridge vulnerable to ground motions with pulse-like components. Specifically, surrogate modeling is applied at the level of quantiles of a scalar response quantity of interest, which is evaluated either with an expensive-to-evaluate high-fidelity or a cheaper low-fidelity stochastic simulator.

As a result, two fragility models associated with a medium damage state are computed for the lateral drift of one of the bridge pier. Accuracy of failure probability estimates is demonstrated by comparison with Monte Carlo simulations of the high-fidelity simulator. The main findings of the benchmark study, which can be reasonably generalized to seismic fragility analysis of bridges, are that:

- Dynamic substructuring and hierarchical kriging provide a mathematically sound framework for balancing computational cost and accuracy of fragility models.
- Polynomial-chaos-based global sensitivity analysis facilitates the selection of the important parameters of the artificial ground motion model to be used as intensity measures for the fragility analysis.
- 200 low-fidelity samples plus 10 high-fidelity samples of response quantiles provide fairly stable fragility models if only the important input parameters are retained.
- 100 realizations of the ground motion model are sufficient to attain fairly stable quantile estimates in the range 0.05 – 0.95 for a given sample of the parameters of the simulator

(both low- and high-fidelity) when displacement-based engineering demand parameters are considered.

- Since polynomial-chaos expansion acts as a denoiser, low-fidelity surrogate models can be computed on noisy quantile estimates obtained with 20 realizations of the ground motion model achieving a considerable reduction of computational cost.
- Any stopping criteria for the adaptive construction of both LF and HF EDs should rely on the convergence of the fragility model instead of the surrogate models.

This study was designed to overcome several limitations present in the current computational fragility practice. Since the proposed methodological approach is in its infancy, room for important advancements is identified in the areas of i) surrogate modeling for stochastic simulators ii) dimensionality reduction for stochastic ground motions models iii) optimal experimental design for the validation of high-fidelity models.

## Appendix A. PCE-based Sobol' sensitivity indices

Assume that the vector of input variables  $\mathbf{X}$  has support  $\mathcal{D}_{\mathbf{X}}$  and follows an independent joint PDF  $f_{\mathbf{X}}(\mathbf{X}) = \prod_m^M f_{X_m}(x_m)$  where  $f_{X_m}$  is the marginal PDF of the  $m$ -th input variable. Any square-integrable mapping  $Y = \mathcal{M}(\mathbf{X})$  w.r.t. the probability measure associated with  $f_{\mathbf{X}}$ , can be written as a sum of functions of increasing dimension as (Sobol, 1993):

$$\mathcal{M}(\mathbf{X}) = \mathcal{M}_0 + \sum_{m=1}^M \mathcal{M}_m(X_m) + \sum_{1 \leq m \leq l \leq M} \mathcal{M}_{m,l}(X_m, X_l) + \dots + \mathcal{M}_{1,2,\dots,M}(\mathbf{X}), \quad (\text{A.1})$$

or equivalently:

$$\mathcal{M}(\mathbf{X}) = \mathcal{M}_0 + \sum_{\mathbf{u} \neq \emptyset} \mathcal{M}_{\mathbf{u}}(\mathbf{X}_{\mathbf{u}}), \quad (\text{A.2})$$

where  $\mathcal{M}_0$  is the mean value of  $Y$ ,  $\mathbf{u} = \{m_1, \dots, m_s\} \subset \{1, \dots, M\}$  are index sets, and  $\mathbf{X}_{\mathbf{u}}$  denotes a subvector of  $\mathbf{X}$  containing only the components indexed by  $\mathbf{u}$ . The number of summands in the above equation is  $2^M - 1$ . The uniqueness and orthogonality of Sobol'-Hoeffding decomposition allow for the following decomposition of the variance  $D$  of  $Y$ :

$$D = \text{Var}[\mathcal{M}(\mathbf{X})] = \sum_{\mathbf{u} \neq \emptyset} \mathcal{D}_{\mathbf{u}} \quad (\text{A.3})$$

where  $\mathcal{D}_{\mathbf{u}}$  denotes the partial variance:

$$\mathcal{D}_{\mathbf{u}} = \text{Var}[\mathcal{M}_{\mathbf{u}}(\mathbf{X}_{\mathbf{u}})] = \mathbb{E}[\mathcal{M}_{\mathbf{u}}^2(\mathbf{X}_{\mathbf{u}})]. \quad (\text{A.4})$$

The Sobol' index  $S_{\mathbf{u}}$  can be defined as the fraction of the total variance  $D_{\mathbf{u}}$  that corresponds to the set of input variables indexed by  $\mathbf{u}$ :

$$S_{\mathbf{u}} = \frac{\mathcal{D}_{\mathbf{u}}}{D}. \quad (\text{A.5})$$

By construction,  $\sum_{\mathbf{u} \neq \emptyset} S_{\mathbf{u}} = 1$ . First-order indices  $S_m^{(1)}$  describe the influence of each parameters  $X_m$  considered separately. Second-order indices  $S_{ml}^{(2)}$  describe the influence from pairs of parameters  $\{X_m, X_l\}$  not already accounted for by  $X_m$  or  $X_l$  separately. High-order indices combine influences from larger sets of parameters. The total sensitivity indices  $S_m^{(\text{tot})}$  represent

the total effect of an input variable  $X_m$  accounting for its main effect and all interactions with other input variables. It follows that  $S_m^{(\text{tot})} = 1 - S_{\sim m}$ , where  $S_{\sim m}$  is the sum of all  $S_{\mathbf{u}}$  with  $\mathbf{u}$  not including  $m$ . Sobol' indices can be evaluated by Monte Carlo simulation (Saltelli et al., 2007), which requires  $\mathcal{O}(10^3)$  model evaluations for each index  $S_{\mathbf{u}}$ . Sobol' indices can be obtained analytically at no additional cost than computing the PCE. A concise description of PCE-based Sobol' sensitivity indices estimation is given herein; for further details, the reader is referred to (Sudret, 2008; Gratiot et al., 2015).

PCE relies on the decomposition of  $Y = \mathcal{M}(\mathbf{X})$ , as a linear superposition of non-linear functions as follows:

$$\hat{Y} = \mathcal{M}^{\text{PCE}}(\mathbf{X}) = \sum_{\alpha \in \mathcal{A}} y_{\alpha} \Psi_{\alpha}(\mathbf{X}), \quad (\text{A.6})$$

where  $\{\Psi_{\alpha}, \alpha \in \mathcal{A}\}$  is a set of multivariate polynomials that are orthogonal w.r.t. the input vector with independent components  $\mathbf{X} \sim f_{\mathbf{X}}(\mathbf{X}) = \prod_{m=1}^M f_{\mathbf{X}_m}(\mathbf{X}_m)$ ,  $\alpha = (\alpha_1, \dots, \alpha_M)$  is a multi-index that identifies the polynomial degree in each of the input variables, and  $y_{\alpha}$  denotes the corresponding polynomial coefficient (coordinate). Following the orthonormality condition,  $\mathbb{E}[\mathcal{M}^{\text{PCE}}(\mathbf{X})] = y_0$ . For practical purposes, the infinite sum in Eq.A.6 needs to be truncated to a finite series. This is commonly achieved by maximum-degree or hyperbolic norm truncation (for more details, see (Blatman and Sudret, 2011)). In order to compute the PCE, first, a so-called ED, consisting of a set of realization of the input vector  $\mathbf{X} = \{\mathbf{x}^{(1)}, \dots, \mathbf{x}^{(N)}\}$  and the corresponding model evaluations  $\mathcal{Y} = \{y^{(1)}, \dots, y^{(N)}\}$ , is generated. Then, the set of coefficients  $y_{\alpha}$  is estimated by minimizing the expected mean-square approximation error on the ED by solving:

$$\hat{y}_{\alpha} = \arg \min_{y_{\alpha}} \mathbb{E} \left[ \left( Y - \hat{Y} \right)^2 \right] \quad (\text{A.7})$$

In the present application, the ED was formed by sampling the input variable space with a Sobol' low-discrepancy sequence. The minimization in Eq.A.7 was solved using the hybrid least angle regression method originally proposed in (Blatman and Sudret, 2011). It is straightforward to obtain the Sobol' decomposition of  $Y$  in an analytical form by observing that the summands  $\mathcal{M}_{\mathbf{u}}^{\text{PCE}}(\mathbf{X}_{\mathbf{u}})$  in Eq.A.2 can be written as:

$$\mathcal{M}_{\mathbf{u}}^{\text{PCE}}(\mathbf{X}_{\mathbf{u}}) = \sum_{\alpha \in \mathcal{A}_{\mathbf{u}}} y_{\alpha} \Psi_{\alpha}(\mathbf{X}_{\mathbf{u}}), \quad (\text{A.8})$$

where  $\mathcal{A}_{\mathbf{u}} = \{\alpha \in \mathcal{A} : \alpha_k \neq 0 \text{ if and only if } k \in \mathbf{u}\}$  denotes the set of multi-indices such that  $\cup \mathcal{A}_{\mathbf{u}} = \mathcal{A}$ . Consequently, due to the uniqueness of Sobol'-Hoeffding decomposition, there is an analytical expression of  $\mathcal{M}_{\mathbf{u}}^{\text{PCE}}$  of Eq.A.8, which serves as a proxy of  $\mathcal{M}_{\mathbf{u}}$ . The analytical expression of the total variance of a PCE is given by (Xiu and Karniadakis, 2002):

$$D = \text{Var} [\mathcal{M}^{\text{PCE}}(\mathbf{X})] = \sum_{\alpha \in \mathcal{A}} y_{\alpha}^2. \quad (\text{A.9})$$

Similarly, the partial variance  $D_{\mathbf{u}}$  reads:

$$D_{\mathbf{u}} = \text{Var} [\mathcal{M}_{\mathbf{u}}^{\text{PCE}}(\mathbf{X}_{\mathbf{u}})] = \sum_{\alpha \in \mathcal{A}_{\mathbf{u}}} y_{\alpha}^2. \quad (\text{A.10})$$

Accordingly, the Sobol' indices of any order can be approximated by a simple combination of the squares of the PCE coefficients by substituting Eqs.A.10 and A.9 in Eq.A.5. For instance, the first-order Sobol' indices, which describe the influence of each input variable  $\mathbf{X}_m$  considered separately, read:

$$S_m^{(1)} = \frac{\sum_{\alpha \in \mathcal{A}_m} y_{\alpha}^2}{\sum_{\alpha \in \mathcal{A}} y_{\alpha}^2}, \quad \mathcal{A}_m = \{\alpha \in \mathcal{A} : \alpha_m > 0, \alpha_{m \neq l} = 0\} \quad (\text{A.11})$$

whereas the total Sobol' indices, which represent the total effect of an input variable  $\mathbf{X}_m$  accounting for its main effect and all interaction with other input variables, are given by:

$$S_m^{(\text{tot})} = \frac{\sum_{\alpha \in \mathcal{A}_m^{\text{tot}}} y_\alpha^2}{\sum_{\alpha \in \mathcal{A}} y_\alpha^2}, \quad \mathcal{A}_m^{\text{tot}} = \{\alpha \in \mathcal{A} : \alpha_m > 0\}. \quad (\text{A.12})$$

Sobol' indices provide quantitative insight on the importance of an input variable. However, they do not include information about the direction in which an input variable affects the model response  $Y$ . So-called univariate effects can answer this question (Deman et al., 2016; Harenberg et al., 2019). A univariate effect is the expectation of  $Y$  conditioned on the value of a single input variable. Univariate effects have a closed analytical form for PCE models, closely related to the first-order Sobol' decomposition,

$$\mathcal{M}_m^{(1)}(X_m) = \sum_{\alpha \in \mathcal{A}_m} y_\alpha \Psi_\alpha(X_m), \quad \mathcal{A}_m = \{\alpha \in \mathcal{A} : \alpha_m > 0, \alpha_{m \neq l} = 0\} \quad (\text{A.13})$$

In this study, computations of both PCE and Sobol' indices were performed using UQLAB, which is a MATLAB toolbox for UQ developed by the Chair of Risk, Safety and Uncertainty Quantification of ETH Zurich (Marelli and Sudret, 2014, 2019; Marelli et al., 2019).

## Appendix B. HK surrogate modeling

Let  $\{\mathcal{M}_c, c = 1, \dots, C\}$  being a series of simulators sorted by increasing level of fidelity, and  $y_c$  the associated output,  $y_c = \mathcal{M}_c(\mathbf{x})$ . In addition, let  $\hat{\mathcal{M}}_c^K$  define the Kriging surrogate model of the simulator  $\mathcal{M}_c(\mathbf{x})$ . A Kriging surrogate model is defined as an infinite collection of jointly Gaussian random variables (i.e., a Gaussian stochastic process). Any finite sample of the process is a Gaussian random vector, which is completely defined by the multivariate Gaussian distribution (Rasmussen and Williams, 2006). In this context, the input  $\mathbf{X}$  is sampled at  $N_c$  distinct locations within the support  $\mathcal{D}_\mathbf{X}$ , and the corresponding scalar output are  $\{y_c^{(n)} = \mathcal{M}_c(\mathbf{x}_c^{(n)}), n = 1, \dots, N_c\}$ . The  $N_c$  distinct input samples are collected in the set  $\mathcal{X}_c = \{\mathbf{X}^{(1)}, \dots, \mathbf{X}^{(N_c)}\}^T$  and the output in the set  $\mathcal{Y}_c = \{y_c^{(1)}, \dots, y_c^{(N_c)}\}^T$ . Here, the set  $\mathcal{Y}_c$  is considered as realization of a Gaussian random vector,  $\mathbf{Y}_c = [Y^{(1)}, \dots, Y^{(N_c)}]^T$ , with mean  $\mu_c(\mathbf{X})$ , and covariance matrix  $\Sigma_c(\mathbf{X})$ . Therefore, the kriging surrogate model of the  $c$  simulator can be defined as (Cressie, 1992; Santner et al., 2003; Rasmussen and Williams, 2006)

$$\begin{aligned} \mathcal{M}_c(\mathbf{X}) &\approx \hat{\mathcal{M}}_c^K(\mathbf{X}) = \mu_c(\mathbf{X}) + \sigma_c^2 Z(\mathbf{X}), \\ &= \mathbf{f}_c(\mathbf{X})^T \boldsymbol{\beta}_c + \sigma_c^2 Z(\mathbf{X}), \end{aligned} \quad (\text{B.1})$$

where  $\boldsymbol{\beta}_c$  is a vector of regression coefficients,  $\mathbf{f}_c(\mathbf{X})$  is a vector collecting a series of basis functions,  $\sigma_c^2$  is the variance of the process, and  $Z(\mathbf{X})$  is a zero-mean, unit-variance stationary Gaussian process. Therefore,  $Z(\mathbf{X})$  is fully determined by the correlation function  $R(\mathbf{X}, \mathbf{X}' | \boldsymbol{\theta}) = R(\mathbf{X} - \mathbf{X}' | \boldsymbol{\theta})$  between two distinct points  $(\mathbf{X}, \mathbf{X}')$  in the input space, where  $\boldsymbol{\theta}$  is a set of hyper-parameters. Given the input ED  $\mathcal{X}_c$  and the output set  $\mathcal{Y}_c$ ,  $\boldsymbol{\beta}_c$ ,  $\boldsymbol{\theta}_c$ , and  $\sigma_c$  are generally determined by generalized least squares as follow (Santner et al., 2003; Dubourg, 2011):

$$\hat{\boldsymbol{\theta}}_c = \arg \min_{A_{\mathcal{D}_\theta}} \left[ \frac{1}{2} \log(\det(\mathbf{R})) + \frac{n}{2} \log(2\pi\sigma_c^2) + \frac{n}{2} \right], \quad (\text{B.2})$$

$$\hat{\boldsymbol{\beta}}_c(\hat{\boldsymbol{\theta}}_c) = (\mathbf{F}_c^T \mathbf{R}^{-1} \mathbf{F}_c)^{-1} \mathbf{F}_c^T \mathbf{R}^{-1} \mathcal{Y}_c, \quad (\text{B.3})$$

$$\hat{\sigma}_c^2(\hat{\boldsymbol{\theta}}_c) = \frac{(\mathcal{Y}_c - \mathbf{F}_c \hat{\boldsymbol{\beta}}_c)^T \mathbf{R}^{-1} (\mathcal{Y}_c - \mathbf{F}_c \hat{\boldsymbol{\beta}}_c)}{N_c}, \quad (\text{B.4})$$

where  $R_{n,m} = \mathbf{R}(\mathbf{X}^n, \mathbf{X}^m)$  is the correlation matrix between the  $N_c$  samples, and  $\mathbf{F}_c = [\mathbf{f}_c(\mathbf{X}^{(1)}), \dots, \mathbf{f}_c(\mathbf{X}^{(N_c)})]^T$  is the information matrix. Next, given a desired test point  $\mathbf{x}^*$ , the random variable of the unobserved output  $Y_c^* | \mathcal{X}_c, \mathcal{Y}_c = \mathcal{M}_c^K(\mathbf{x}^* | \mathcal{X}_c, \mathcal{Y}_c)$  has conditional Gaussian distribution (Santner et al., 2003) with parameters

$$\begin{aligned} \mu_{y_c^*} &= \mathbb{E} \left[ Y_c^* \mid \mathcal{X}_c, \mathcal{Y}_c \right], \\ &= \mathbf{f}_c(\mathbf{x}^*)^T \hat{\boldsymbol{\beta}}_c + \mathbf{r}^T(\mathbf{x}^*) \mathbf{R}^{-1} \left( \mathcal{Y}_c - \mathbf{F}_c \hat{\boldsymbol{\beta}}_c \right), \end{aligned} \quad (\text{B.5})$$

$$\begin{aligned} \sigma_{y_c^*}^2 &= \text{Var} \left[ Y_c^* \mid \mathcal{X}_c, \mathcal{Y}_c \right], \\ &= \hat{\sigma}_c^2 \left[ 1 - \mathbf{r}^T(\mathbf{x}^*) \mathbf{R}^{-1} \mathbf{r}(\mathbf{x}^*) + (\mathbf{F}_c^T \mathbf{R}^{-1} \mathbf{r}(\mathbf{x}^*) - \mathbf{f}_c(\mathbf{x}^*))^T (\mathbf{F}_c^T \mathbf{R}^{-1} \mathbf{F}_c)^{-1} (\mathbf{F}_c^T \mathbf{R}^{-1} \mathbf{r}(\mathbf{x}^*) - \mathbf{f}_c(\mathbf{x}^*)) \right], \end{aligned} \quad (\text{B.6})$$

where  $\mathbf{r}(\mathbf{x}^*) = \hat{\boldsymbol{\theta}}_c = [R(\mathbf{x}^* - \mathbf{x}^{(1)} | \hat{\boldsymbol{\theta}}_c), \dots, R(\mathbf{x}^* - \mathbf{x}^{(N_c)} | \hat{\boldsymbol{\theta}}_c)]^T$  is the cross-correlation vector between the point  $\mathbf{x}^*$  and each of the points of  $\mathcal{X}_c$ . In this study, we use a nested combination of surrogate models to define a HK surrogate (Abdallah et al., 2019). Specifically, a PCE surrogate of the LF simulator is used as a trend for the kriging surrogate of the HF simulator. For the two levels  $c \in [LF, HF]$ , the HK predictor at an unobserved point  $\mathbf{x}^*$  can be written as (Han and Görtz, 2012):

$$\mu_{y_{HF}^*} = \hat{\mathcal{M}}_{LF}^{PCE}(\mathbf{x}^*) \hat{\boldsymbol{\beta}}_{HF} + \mathbf{r}(\mathbf{x}^*)^T \mathbf{R}^{-1} (\mathcal{Y}_{HF} - \mathbf{F}_{LF} \hat{\boldsymbol{\beta}}_{HF}), \quad (\text{B.7})$$

where  $\hat{\mathcal{M}}_{LF}^{PCE}(\mathbf{x}^*)$  is PCE surrogate of the LF simulator,  $\mathcal{Y}_{HF}$  is the vector of output from the HF simulator,  $\mathbf{F}_{LF} = [\mathcal{M}_{LF}(\mathbf{x}_1), \dots, \mathcal{M}_{LF}(\mathbf{x}_{N_c})]$ , and  $\hat{\boldsymbol{\beta}}_{HF}$  is a constant. The variance of the HK predictor is similar to Eq.B.6, i.e.

$$\begin{aligned} \sigma_{y_{HF}^*}^2 &= \hat{\sigma}_{HF}^2 \left[ 1 - \mathbf{r}(\mathbf{x}^*)^T \mathbf{R}^{-1} \mathbf{r}(\mathbf{x}^*) + \right. \\ &\quad \left. (\mathbf{F}_{LF}^T \mathbf{R}^{-1} \mathbf{r}(\mathbf{x}^*) - \hat{\mathcal{M}}_{LF}^{PCE}(\mathbf{x}^*))^T (\mathbf{F}_{LF}^T \mathbf{R}^{-1} \mathbf{F}_{LF})^{-1} (\mathbf{F}_{LF}^T \mathbf{R}^{-1} \mathbf{r}(\mathbf{x}^*) - \hat{\mathcal{M}}_{LF}^{PCE}(\mathbf{x}^*)) \right]. \end{aligned} \quad (\text{B.8})$$

In this study, computations of kriging surrogates were performed using UQLAB, which is a MATLAB toolbox for UQ developed by the Chair of Risk, Safety and Uncertainty Quantification of ETH Zurich (Marelli and Sudret, 2014; Lataniotis et al., 2019).

## Acknowledgments

The authors wish to acknowledge the Chair of Structural Dynamics and Earthquake Engineering (Prof. Dr. Božidar Stojadinović), the Chair of Risk, Safety and UQ (Prof. Dr. Bruno Sudret) and the Chair of Structural Mechanics (Prof. Dr. Eleni Chatzi) of ETH Zurich, Switzerland, for having supported this research. The second author was supported by the Italian Ministry of Education, University and Research (MIUR) in the frame of the ‘‘Departments of Excellence’’ (grant L. 232/2016).

## References

Abbiati, G., O. S. Bursi, P. Caperan, L. Di Sarno, F. J. Molina, F. Paolacci, and P. Pegon (2015). Hybrid simulation of a multi-span RC viaduct with plain bars and sliding bearings: Hybrid Simulations of a Multi-Span RC Viaduct. *Earthquake Engineering & Structural Dynamics* 44(13), 2221–2240.

- Abdallah, I., C. Lataniotis, and B. Sudret (2019). Parametric hierarchical kriging for multi-fidelity aero-servo-elastic simulators — Application to extreme loads on wind turbines. *Probabilistic Engineering Mechanics* 55, 67–77.
- Alessandri, S., R. Giannini, and F. Paolacci (2013). Aftershock risk assessment and the decision to open traffic on bridges. *Earthquake Engineering & Structural Dynamics* 42(15), 2255–2275.
- Altieri, D. and E. Patelli (2020). An efficient approach for computing analytical non-parametric fragility curves. *Structural Safety* 85, 101956.
- Baker, J. W. (2007). Quantitative classification of near-fault ground motions using wavelet analysis. *Bulletin of the Seismological Society of America* 97(5), 1486–1501.
- Baker, J. W. (2011). Conditional Mean Spectrum: Tool for Ground-Motion Selection. *Journal of Structural Engineering* 137(3), 322–331.
- Baker, J. W. (2015). Efficient analytical fragility function fitting using dynamic structural analysis. *Earthquake Spectra* 31(1), 579–599.
- Bazzurro, P. and C. Allin Cornell (1999). Disaggregation of seismic hazard. *Bulletin of the Seismological Society of America* 89(2), 501–520.
- Blatman, G. and B. Sudret (2011). Adaptive sparse polynomial chaos expansion based on least angle regression. *Journal of Computational Physics* 230(6), 2345–2367.
- Bradley, B. A. (2010). A generalized conditional intensity measure approach and holistic ground-motion selection. *Earthquake Engineering & Structural Dynamics*, n/a–n/a.
- Bradley, B. A. (2013). A critical examination of seismic response uncertainty analysis in earthquake engineering. *Earthquake Engineering & Structural Dynamics* 42(11), 1717–1729.
- Bursi, O. S., G. Abbiati, E. Cazzador, P. Pegon, and F. J. Molina (2017). Nonlinear heterogeneous dynamic substructuring and partitioned FETI time integration for the development of low-discrepancy simulation models. *International Journal for Numerical Methods in Engineering* 112(9), 1253–1291.
- Craig, R. R. and A. J. Kurdila (2006). *Fundamentals of structural dynamics*. John Wiley & Sons.
- Cressie, N. (1992). *Statistics for spatial data*, Volume 4. Wiley Online Library.
- Dabaghi, M. and A. D. Kiureghian (2017). Stochastic model for simulation of near-fault ground motions. *Earthquake Engineering & Structural Dynamics* 46(6), 963–984.
- de Klerk, D., D. J. Rixen, and S. N. Voormeeren (2008). General Framework for Dynamic Substructuring: History, Review and Classification of Techniques. *AIAA Journal* 46(5), 1169–1181.
- Deman, G., K. Konakli, B. Sudret, J. Kerrou, P. Perrochet, and H. Benabderrahmane (2016). Using sparse polynomial chaos expansions for the global sensitivity analysis of groundwater lifetime expectancy in a multi-layered hydrogeological model. *Reliability Engineering & System Safety* 147, 156–169.
- Dubourg, V. (2011). *Adaptive surrogate models for reliability analysis and reliability-based design optimization*. Ph. D. thesis, Universite’ Blaise Pascal, Clermont-Ferrand II.

- Ghosh, S., A. Roy, and S. Chakraborty (2019). Kriging Metamodeling-Based Monte Carlo Simulation for Improved Seismic Fragility Analysis of Structures. *Journal of Earthquake Engineering*, 1–21.
- Gidaris, I., A. A. Taflanidis, and G. P. Mavroeidis (2015). Kriging metamodeling in seismic risk assessment based on stochastic ground motion models: Seismic Risk Assessment Through Kriging Metamodeling. *Earthquake Engineering & Structural Dynamics* 44 (14), 2377–2399.
- Gratiet, L. L., S. Marelli, and B. Sudret (2015). Metamodel-Based Sensitivity Analysis: Polynomial Chaos Expansions and Gaussian Processes. In R. Ghanem, D. Higdon, and H. Owhadi (Eds.), *Handbook of Uncertainty Quantification*, pp. 1–37. Cham: Springer International Publishing.
- Grigoriu, M. (2011). To Scale or Not to Scale Seismic Ground-Acceleration Records. *Journal of Engineering Mechanics* 137(4), 284–293.
- Han, Z.-H. and S. Görtz (2012). Hierarchical Kriging Model for Variable-Fidelity Surrogate Modeling. *AIAA Journal* 50(9), 1885–1896.
- Harenberg, D., S. Marelli, B. Sudret, and V. Winschel (2019). Uncertainty quantification and global sensitivity analysis for economic models. *Quantitative Economics* 10(1), 1–41.
- Iervolino, I., C. Galasso, and E. Cosenza (2010). REXEL: computer aided record selection for code-based seismic structural analysis. *Bulletin of Earthquake Engineering* 8(2), 339–362.
- Ikhouane, F. and J. Rodellar (2007). *Systems with hysteresis: analysis, identification and control using the Bouc-Wen model*. Chichester, England ; Hoboken, NJ: John Wiley.
- Lataniotis, C., D. Wicaksono, S. Marelli, and B. Sudret (2019). UQLab user manual – Kriging (Gaussian process modeling). Technical report, Chair of Risk, Safety and Uncertainty Quantification, ETH Zurich, Switzerland.
- Le Gratiet, L., S. Marelli, and B. Sudret (2017). *Metamodel-Based Sensitivity Analysis: Polynomial Chaos Expansions and Gaussian Processes*, pp. 1289–1325. Cham: Springer International Publishing.
- Mai, C., K. Konakli, and B. Sudret (2017). Seismic fragility curves for structures using non-parametric representations. *Frontiers of Structural and Civil Engineering* 11(2), 169–186.
- Marelli, S., C. Lamas, K. Konakli, C. Mylonas, P. Wiederkehr, and B. Sudret (2019). UQLab user manual – Sensitivity analysis. Technical report, Chair of Risk, Safety and Uncertainty Quantification, ETH Zurich, Switzerland.
- Marelli, S. and B. Sudret (2014). UQLab: A Framework for Uncertainty Quantification in Matlab. In *Vulnerability, Uncertainty, and Risk*, Liverpool, UK, pp. 2554–2563. American Society of Civil Engineers.
- Marelli, S. and B. Sudret (2019). UQLab user manual – Polynomial chaos expansions. Technical report, Chair of Risk, Safety and Uncertainty Quantification, ETH Zurich, Switzerland.
- Mavroeidis, G. P. (2003). A Mathematical Representation of Near-Fault Ground Motions. *Bulletin of the Seismological Society of America* 93(3), 1099–1131.
- McKenna, F., M. H. Scott, and G. L. Fenves (2010). Nonlinear Finite-Element Analysis Software Architecture Using Object Composition. *Journal of Computing in Civil Engineering* 24(1), 13.

- Ng, L. W.-T. and M. Eldred (2012). *Multifidelity Uncertainty Quantification Using Non-Intrusive Polynomial Chaos and Stochastic Collocation*.
- Noh, H. Y., D. Lallemand, and A. S. Kiremidjian (2015). Development of empirical and analytical fragility functions using kernel smoothing methods. *Earthquake Engineering & Structural Dynamics* 44(8), 1163–1180.
- Pacor, F., R. Paolucci, L. Luzi, F. Sabetta, A. Spinelli, A. Gorini, M. Nicoletti, S. Marcucci, L. Filippi, and M. Dolce (2011). Overview of the Italian strong motion database ITACA 1.0. *Bulletin of Earthquake Engineering* 9(6), 1723–1739.
- Paolacci, F. and R. Giannini (2012). An experimental and numerical investigation on the cyclic response of a portal frame pier belonging to an old reinforced concrete viaduct. *Earthquake Engineering & Structural Dynamics* 41(6), 1109–1127.
- Paolacci, F., F. J. Molina, R. Giannini, L. Di Sarno, G. Abbiati, A. Mohamad, O. Bursi, F. Taucer, R. Ceravolo, P. Pegon, M. Poljansek, L. Zanotti Fragonara, M. Sartori, S. Alessandri, R. De Risi, and C. Yenidogan (2014). Assessment of the seismic vulnerability of an old RC viaduct with frame piers and study of the effectiveness of base isolation through PsD testing (RETRO). Technical report, Publications Office, Luxembourg.
- Porter, K., R. Kennedy, and R. Bachman (2007). Creating fragility functions for performance-based earthquake engineering. *Earthquake Spectra* 23.
- Rasmussen, C. E. and C. K. I. Williams (2006). *Gaussian processes in machine learning*. Cambridge, Massachusetts: MIT Press.
- Rezaeian, S. and A. Der Kiureghian (2008). A stochastic ground motion model with separable temporal and spectral nonstationarities. *Earthquake Engineering & Structural Dynamics* 37(13), 1565–1584.
- Rezaeian, S. and A. Der Kiureghian (2010). Simulation of synthetic ground motions for specified earthquake and site characteristics. *Earthquake Engineering & Structural Dynamics*, n/a–n/a.
- Saltelli, A., M. Ratto, T. Andres, F. Campolongo, J. Cariboni, D. Gatelli, M. Saisana, and S. Tarantola (2007). *Global Sensitivity Analysis. The Primer*. Chichester, UK: John Wiley & Sons, Ltd.
- Santner, T., B. Williams, and W. Notz (2003). *The design and analysis of computer experiments*. New York, NY: Springer.
- Schellenberg, A. H., S. A. Mahin, and G. L. Fenves (2009). Advanced Implementation of Hybrid Simulation. Technical Report PERR 2009/104, Pacific Earthquake Engineering Research (PEER) Center, University of California, Berkeley.
- Silva, V., S. Akkar, J. Baker, P. Bazzurro, J. M. Castro, H. Crowley, M. Dolsek, C. Galasso, S. Lagomarsino, R. Monteiro, D. Perrone, K. Pitilakis, and D. Vamvatsikos (2019). Current Challenges and Future Trends in Analytical Fragility and Vulnerability Modeling. *Earthquake Spectra* 35(4), 1927–1952.
- Sobol, I. M. (1993). Sensitivity estimates for nonlinear mathematical models. *Mathematical modelling and computational experiments* 1(4), 407–414.
- Stefanou, G. (2009, February). The stochastic finite element method: Past, present and future. *Computer Methods in Applied Mechanics and Engineering* 198(9-12), 1031–1051.

- Sudret, B. (2008). Global sensitivity analysis using polynomial chaos expansions. *Reliability Engineering & System Safety* 93(7), 964–979.
- Suzuki, A. and I. Iervolino (2020). Intensity measure conversion of fragility curves. *Earthquake Engineering & Structural Dynamics* 49(6), 607–629.
- Torre, E., S. Marelli, P. Embrechts, and B. Sudret (2019a, July). Data-driven polynomial chaos expansion for machine learning regression. *Journal of Computational Physics* 388, 601–623. ZSCC: 0000023.
- Torre, E., S. Marelli, P. Embrechts, and B. Sudret (2019b). A general framework for data-driven uncertainty quantification under complex input dependencies using vine copulas. *Probabilistic Engineering Mechanics* 55, 1–16.
- Trevlopoulos, K., C. Feau, and I. Zentner (2019). Parametric models averaging for optimized non-parametric fragility curve estimation based on intensity measure data clustering. *Structural Safety* 81, 101865.
- Trucano, T., L. Swiler, T. Igusa, W. Oberkampf, and M. Pilch (2006). Calibration, validation, and sensitivity analysis: What’s what. *Reliability Engineering & System Safety* 91(10-11), 1331–1357.
- Vamvatsikos, D. and C. Cornell (2002). Incremental dynamic analysis. *Earthquake Engineering & Structural Dynamics* 31, 491 – 514.
- Xiu, D. and G. E. Karniadakis (2002). The Wiener–Askey polynomial chaos for stochastic differential equations. *SIAM journal on scientific computing* 24(2), 26.
- Zentner, I. (2017). A general framework for the estimation of analytical fragility functions based on multivariate probability distributions. *Structural Safety* 64, 54–61.